Ore Geology Reviews 75 (2016) 100–115

Contents lists available at ScienceDirect

Ore Geology Reviews

journal homepage: www.elsevier.com/locate/oregeorev

# Genesis of REE minerals in the karstic bauxite in western Guangxi, China, and its constraints on the deposit formation conditions

Xuefei Liu [a], Qingfei Wang [a,*], Qizuan Zhang [b], Ying Zhang [a], Yan Li [a]

[a] State Key Laboratory of Geological Processes and Mineral Resources, China University of Geosciences, Beijing 100083, China
[b] The Bureau of Geo-exploration Guangxi and Mineral Development, Nanning 530023, China

ARTICLE INFO

*Article history:*
Received 22 July 2015
Received in revised form 14 December 2015
Accepted 14 December 2015
Available online 17 December 2015

*Keywords:*
Karstic bauxite
REE minerals
REE mineral genesis
Chemical behavior

ABSTRACT

Karstic bauxites in western Guangxi, China, comprise two subtypes: Permian bauxite and Quaternary bauxite. The Quaternary bauxite originated from the breaking up, rolling, and accumulating of Permian bauxite in karstic depressions in Quaternary. Various types of rare earth element (REE) minerals were discovered during the formation of the Permian and Quaternary bauxites from the Xinxu, Longhe, and Tianyang bauxite deposits in this study. Five types of REE minerals, including bastnäsite, parisite, cerianite, rhabdophane, and churchite, were identified. Bastnäsite and parisite are the most abundant, and they are widely developed in the Permian ore and also present in the Quaternary ore. Obvious variations in bastnäsite and parisite REE compositions were observed, which is ascribed to distinctions in the source materials in the primary weathering profile from different areas. The mode of occurrence of bastnäsite and parisite suggests they were mainly precipitated under alkaline and reducing conditions during the Permian bauxite-forming stage and underwent intensive corrosion in the Quaternary. Churchite was formed during the Permian weathering stage under acidic condition. Both cerianite and rhabdophane occur in fractures within the Permian bauxite ore, indicating that both formed during the Quaternary weathering stage. It is considered that the rhabdophane enriched in Ce have formed locally, in the process of that the $Ce^{3+}$, released from bastnäsite rapidly, entered the rhabdophane lattice before being oxidized to $Ce^{4+}$. Cerianite was mainly found in association with Mn–Al hydroxides, suggesting that the released $Ce^{3+}$ was oxidized into $Ce^{4+}$ and precipitated cerianite in fractures within the Permian bauxite ore. Mass balance equations reveal a depletion in nearly all REEs during the transformation from the Permian to the Quaternary bauxite ore, mainly caused by the dissolution of bastnäsite and parisite. The genesis of the REE minerals, together with the occurrence of other minerals, indicates that intensively acidic and oxidizing conditions developed before the formation of the Permian bauxite ore. Towards the end of the Permian, the conditions became reducing and alkaline, favorable for the large-scale bauxitization. The Quaternary bauxite-forming stage was characterized by variable pH and Eh conditions, with acidic (pH = 4–6) and oxidizing (Eh > 2) conditions at the surface of the exposed Permian bauxite ore.



## 1. Introduction

Rare earth element (REE) minerals are widely developed in bauxitic horizons (Bárdossy et al., 1976; Boulangé et al., 1996; Mordberg, 1996; Mongelli, 1997; Calagari and Abedini, 2007; Wang et al., 2010). Fluorocarbonates of the bastnäsite group minerals (including parisite, rontgenite, and synchysite), cerianite, rhabdophane, and churchite have been identified in bauxite deposits worldwide (Mongelli, 1997; Laskou and Andreou, 2003; Mameli et al., 2007; Wang et al., 2010; Berger et al., 2014; Mongelli et al., 2014). The fluorocarbonates of the bastnäsite group, the most common ones in karstic bauxite deposits, are usually concentrated in the lower section of bauxite deposits as a result of the alkaline condition upon the bedrock limestone, (Maksimovic and Pantó, 1996; Mongelli, 1997; Berger et al., 2014; Mongelli et al., 2014). Cerianite is common in both karstic and lateritic bauxite (Li et al., 2013; Berger et al., 2014). In karstic bauxite deposits, cerianite occurs mainly in the uppermost section of deposits, and has been attributed to the $Ce^{3+} \rightarrow Ce^{4+}$ redox change (Maksimovic and Pantó, 1996; Mongelli, 1997). The rhabdophane mineral group, which generally replaces primary REE minerals in underlying felsic rocks, is common in lateritic profiles, but less so in karstic bauxite (Banfield and Eggleton, 1989; Braun et al., 1990, 1993, 1998; Taunton et al., 2000; Stille et al., 2009; Welch et al., 2009; Ma et al., 2011; Sanematsu et al., 2013). Churchite is generally considered to form in an acidic setting (pH: 0.5–3.0; Hukuo and Hikichi, 1979) and is most common in karstic bauxite (Laskou and Andreou, 2003; Wang et al., 2010; Li et al., 2013). As the precipitation environment (e.g., pH and Eh) of REE minerals in bauxite is well understood, their occurrence and genesis have attracted much attention and they are commonly examined to infer the ore-

* Corresponding author.

http://dx.doi.org/10.1016/j.oregeorev.2015.12.015
0169-1368/

forming conditions and processes (Wang et al., 2010; Li et al., 2013; Berger et al., 2014).

Bauxite deposits in western Guangxi, China, are typically of the karstic type and occur as two subtypes: Permian and Quaternary karstic bauxite (Deng et al., 2010; Liu et al., 2010, 2012; Wang et al., 2010, 2011). Previous studies have attributed the formation of the Quaternary bauxite to the transformation of the Permian bauxite via uplifting, break-up, and accumulation in Quaternary karstic depressions (Deng et al., 2010). The geology, mineralogy, and geochemistry of these deposits, as well as the mineral transformations that occurred during the evolution from the Permian to the Quaternary bauxite, have been widely studied (Liu et al., 2010, 2012; Wang et al., 2011; Yu et al., 2014). Wang et al. (2010) reported two REE minerals (parisite and churchite) in the Permian Xinxu bauxite deposit of western Guangxi and discussed their significance for the paleo-environment for the formation of the deposit. Despite the previous achievement, the type, genesis, and evolution of the REE minerals generated in the process of Permian bauxite formation and Quaternary transformation remain unknown. This paper presents the discovery of the bastnäsite, parisite, rhabdophane, and cerianite REE minerals in the Xinxu, Longhe, and Tianyang bauxite deposits in western Guangxi, and investigates their generations and associated REE behaviors during the transformation from the Permian to the Quaternary bauxite ore. The investigation further clarifies the ore-forming paleo-environment in the various stages.

## 2. Geological background

Western Guangxi is located in the southwestern part of the Youjiang Basin, close to the southwestern margin of the South China block (Fig. 1). The Youjiang Basin extends across southwest China and northeast Vietnam (Deng et al., 2011; Yang et al., 2012a, 2012b). The tectonic extension that created this fault-bound basin was initiated in the Devonian by rifting of Cambrian–Ordovician rocks of the South China block (Du et al., 2009; Yang et al., 2012a, 2012b; Deng et al., 2015a, 2015b). Permian to early Triassic sedimentation within the basin was dominated by marine clastic and volcaniclastic strata with isolated carbonate platforms (Yang et al., 2012a, 2012b). The Permian–Triassic volcanic rocks are found mainly along the south-southwestern margin of the basin and are related to the closure of the Babu Ocean, part of the Paleo-Tethys (Wu et al., 2000, 2002; Yang et al., 2012a; Deng et al., 2014a, 2014b). Several isolated carbonate platforms developed in the Youjiang Basin during the Permian–Triassic (Mei et al., 2007; Yu et al., 2014). Western Guangxi is the site of one such platform, and was uplifted at the end of the middle Permian, possibly a result of the Emeishan plume (Deng et al., 2010; Liu et al., 2010; Wang et al., 2011). The uplift lasted for ca. 3 Ma and may have reached a height of 50–450 m relative to surrounding land surface (He et al., 2003, 2010; Sun et al., 2010).

A large bauxite deposit resulted from the favorable climate and abundant ore-forming materials that weathered from underlying carbonates and magmatic rocks related to the Emeishan plume (Deng et al., 2010; Wang et al., 2010). The Permian bauxitization was terminated by a late Permian transgression that resulted in submergence of the carbonate platforms (Liu et al., 2010). In the Middle–Upper Triassic, clastic detritus infilled the basin, representing the final stage of basin evolution (Du et al., 2009) associated with closure of the Paleo-Tethys (Wu et al., 1999; Cai and Zhang, 2009). Subsequently, the Permian bauxite deposits were folded in the Mesozoic. In the early Cenozoic, under tropical conditions, another stage of weathering began that favored the formation of karst relief. In the late Cenozoic, the Permian

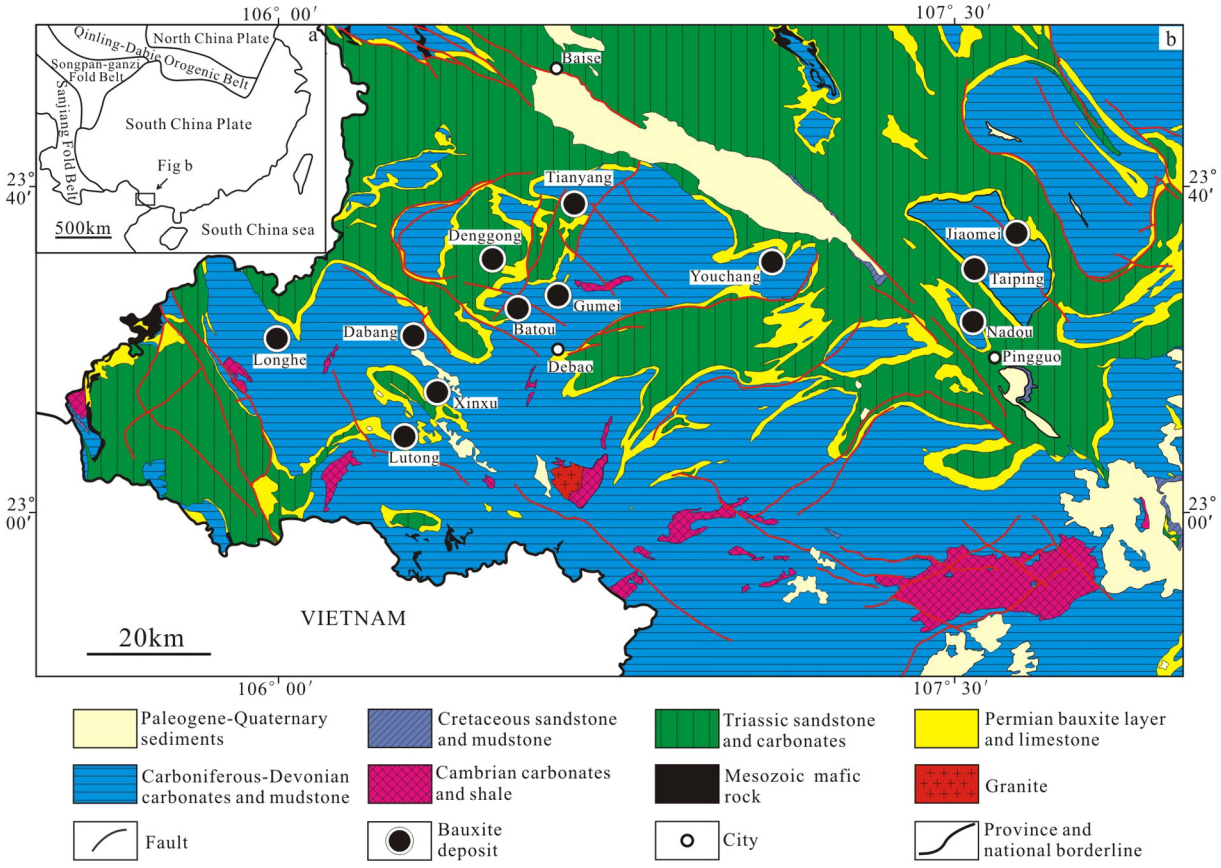


**Fig. 1.** (a) Map showing the location of western Guangxi; (b) simplified geological map of western Guangxi, China, showing the locations of major bauxite deposits. Modified after Deng et al. (2010).

bauxite was exposed, broken up, oxidized, eroded, and re-sedimented into karstic depressions, forming the Quaternary bauxite (Liu et al., 2012; Yu et al., 2014).

The Xinxu, Longhe, and Tianyang bauxite deposits are located in the southwest, west, and northeast parts of the western Guangxi bauxite area, respectively (Fig. 1). The stratigraphic succession of the Xinxu

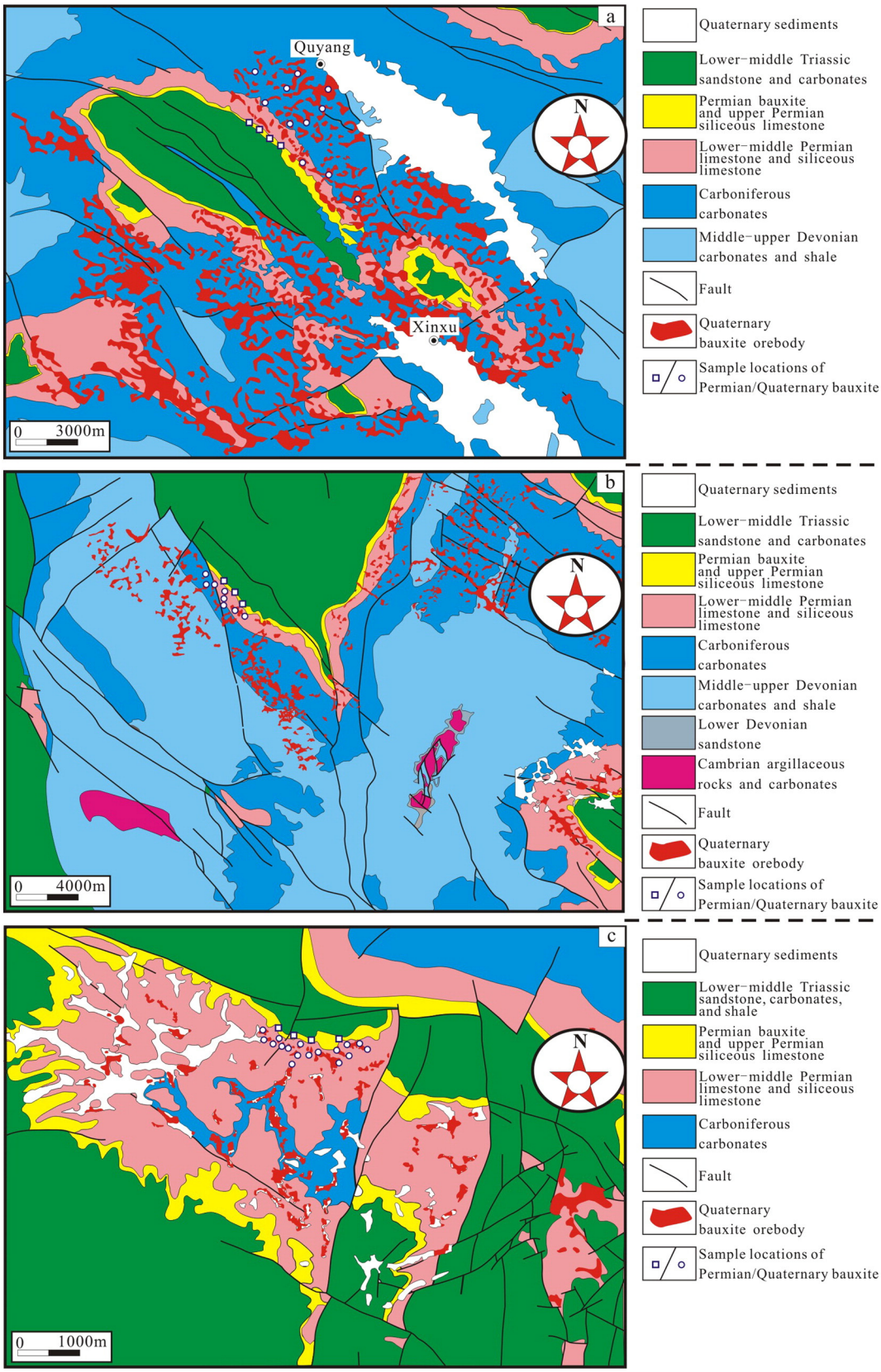


**Fig. 2.** Geological maps of the (a) Xinxu bauxite deposit; (b) Longhe bauxite deposit; (c) and Tianyang bauxite deposit.

bauxite deposit includes (from oldest to youngest) middle to late Devonian carbonates and shale, Carboniferous carbonates, early to middle Permian limestone and siliceous limestone, late Permian siliceous limestone and Permian bauxite ore, early to middle Triassic sandstone and carbonates, and Quaternary sediments and bauxite orebodies (Fig. 2a). The Permian bauxite ore is a 2–5 m thick layer, unconformably overlying the middle Permian Maokou Formation (Fig. 3a; Wang et al., 2010). The Quaternary bauxite ore occurs within lateritic profiles in karstic depressions that formed in the carbonates from the Carboniferous to the middle Permian (Fig. 2a). Three layers (the lower, middle, and upper layers) can be distinguished within the Quaternary lateritic profile (Fig. 3b). The Quaternary bauxite ore is concentrated in the middle layer and ranges from 0 to 25 m in thickness.

The main rock units in the Longhe bauxite deposit include Cambrian argillaceous rocks and carbonates, early Devonian sandstone, middle to late Devonian carbonates and shale, Carboniferous carbonates, early to middle Permian limestone and siliceous limestone, late Permian siliceous limestone, Permian bauxite ore, early to middle Triassic sandstone and carbonates, and Quaternary sediments and bauxite orebodies (Fig. 2b). The Permian bauxite ore overlies the palaeo-karst surface of limestone of the middle Permian Maokou Formation and is overlain by siliceous limestone of the Heshan


**Fig. 3.** Field photographs showing (a) the exposed Permian Xinxu bauxite ore and the Quaternary Xinxu bauxite in the karstic depression; (b) the Quaternary Xinxu bauxite profile; (c) the exposed Permian Longhe bauxite horizon; (d) the Quaternary Longhe bauxite profile; (e) the exposed Permian Tianyang bauxite ore; and (f) the Quaternary Tianyang bauxite profile.

Formation. The bauxite ore is stratiform and varies in thickness (0.5–5.0 m) (Fig. 3c). The Quaternary bauxite ore is located within karstic depressions that developed in the carbonates from the middle Devonian to the middle Permian (Fig. 2b). The Quaternary bauxite ore is up to 29 m thick and occurs in the middle layer of the Quaternary lateritic profile (Fig. 3d).

The strata in the Tianyang bauxite deposit include Carboniferous carbonates, early to middle Permian limestone and siliceous limestone, late Permian siliceous limestone and Permian bauxite ore, early to middle Triassic sandstone, carbonates, and shale, and Quaternary sediments and bauxite orebodies (Fig. 2c). The Permian bauxite ore is 1–4 m thick and is hosted in the lower Heshan Formation, which overlies the palaeokarst surface developed in limestone of the middle Permian Maokou Formation (Fig. 3e). The Quaternary bauxite ore is up to 21 m thick and is hosted in the Quaternary lateritic profile within karstic depressions that developed in carbonates during the Carboniferous to middle Permian (Fig. 2c). The bauxite blocks are randomly scattered in the middle layer (Fig. 3f).

## 3. Sampling and analytical methods

The analyzed samples include both Permian and Quaternary bauxite ore from the Xinxu, Longhe, and Tianyang bauxite deposits. The mineralogy and geochemistry of the Xinxu bauxite deposit have been reported by Wang et al. (2010). We further investigated the same samples as those examined by Wang et al. using X-ray diffraction (XRD) and electron probe microanalysis (EPMA) to understand the mineral composition and the mode of occurrence of REE minerals. Samples of both Permian and Quaternary bauxite ore from Longhe and Tianyang were also collected and analyzed. The samples of Permian bauxite ore were collected from the exposed Permian bauxite horizon. The Quaternary bauxite samples were generally sampled in areas close to where the Permian bauxite is exposed.

To ensure accurate geochemical data, the most strongly weathered sections of the exposed Permian bauxite ore were removed prior to analysis. The samples were crushed in an agate mill and screened through a 200-mesh sieve. All analyzed elements (including major and rare earth elements) were determined at the Geological Survey and Laboratory Center, Langfang, China. Whole-rock abundances of major elements (except FeO) were determined by X-ray fluorescence (XRF) using a Philips Model 1480 spectrometer. FeO contents were analyzed using the volumetric method, and loss on ignition (LOI) was determined using the gravimetric method. The REEs were analyzed using inductively coupled plasma-mass spectrometry (ICP-MS). The detection limit was 0.01 wt.% for major elements (as oxides) and 2 ppm for REEs.

Minerals were identified using XRD and EPMA. XRD analysis was performed at the Petroleum Geology Research and Laboratory Center, Beijing, China (Rigaku D/Mac-RC) using CuKα1 radiation, voltage of 40 kV, beam current of 80 mA, graphite monochromator, continuous scanning, scanning speed of 8°/min, slit DS = SS = 1°, ambient temperature of 18 °C, and humidity of 30%.

Major and trace elements abundances were measured using a Shimadzu EPMA-1720 electron probe microanalyzer (EPMA) at the China University of Geosciences in Beijing. Operating conditions were an accelerating voltage of 15 kV, beam current of 10 nA, beam lifetime of 50 s, and beam diameter of 1 μm. The Kα X-ray line was used for the elements Si, Fe, Ca, P, F, Al, Na, Mg, Ti, and Mn, the Lα line for Y, La, Ce, Pr, Nd, Sm, Eu, Gd, Dy, Ho, Er, Tm, and Yb, and the Mα line for Tb. Albite (Na, Al, and Si), apatite (Ca and P), rutile (Ti), rhodonite (Mn), magnetite (Fe), olivine (Mg), zircon (Y), fluorite (F), and synthetic REE–phosphates (La, Ce, Pr, Nd, Sm, Eu, Gd, Tb, Dy, Ho, Er, Tm, and Yb) were used as reference standards. The synthetic REE–phosphates used for REEs have been described in detail by Liu et al. (2015a, 2015b). The precision was better than 5% for elements with concentrations of >20 wt.%, better than 10% for concentrations of 3 wt.% to 20 wt.%, better than 30% for concentrations of 1 to 3 wt.%, and better than 50% for concentrations of 0.5 to 1 wt.% (Yin et al., 2013).

## 4. Ore geochemistry

The major and rare earth element compositions of the Permian and Quaternary bauxite ores of the Longhe and Tianyang deposits are listed in Table 1.

### 4.1. Geochemical compositions

In the Quaternary bauxite ore of the Longhe deposit, $Al_2O_3$ ranges from 38.13 to 53.58 wt.%, $Fe_2O_3$ from 25.44 to 33.79 wt.%, $SiO_2$ from 0.71 to 17.65 wt.%, $TiO_2$ from 2.07 to 5.46 wt.%, and FeO from 0.12 to 0.52 wt.%. In the Permian bauxite ore of the Longhe deposit, $Al_2O_3$ ranges from 49.40 to 57.42 wt.%, $Fe_2O_3$ from 7.88 to 16.98 wt.%, FeO from 5.30 to 12.85 wt.%, $SiO_2$ from 7.73 to 9.82 wt.%, and $TiO_2$ from 2.45 to 4.17 wt.%. The Quaternary bauxite ore contains variable REE contents of 151.98–799.18 ppm (average of 388.92 ppm), LREE contents of 98.14–709.22 ppm (average of 328.04 ppm), and HREE contents of 47.39–89.96 ppm (average of 60.89 ppm; Fig. 4a). The Quaternary bauxite ore shows generally positive Ce anomalies (0.58–2.01) and negative Eu anomalies (0.46–0.68). The Permian bauxite ore shows clear enrichments in REE, LREE, and HREE relative to the Quaternary bauxite ore (Fig. 4a). The REE, LREE, and HREE in the Permian bauxite ore are 479.69–1035.23 ppm (average of 818.86), 411.63–996.51 ppm (average of 747.45), and 38.72–107.45 ppm (average of 71.41), respectively. The Ce and Eu anomalies range from 1.11 to 5.16 and 0.48 to 0.56, respectively.

In the Quaternary ore of the Tianyang bauxite deposit, $Al_2O_3$ ranges from 27.15 to 75.94 wt.%, $Fe_2O_3$ from 1.21 to 42.16 wt.%, FeO from 0.08 to 9.35 wt.%, $SiO_2$ from 0.29 to 15.70 wt.%, and $TiO_2$ from 2.76 to 6.86 wt.%. In the Permian bauxite ore, $Al_2O_3$ ranges from 34.12 to 59.05 wt.%, $Fe_2O_3$ from 5.15 to 9.48 wt.%, FeO from 9.32 to 21.36 wt.%, $SiO_2$ from 6.63 to 19.77 wt.%, and $TiO_2$ from 3.86 to 4.21 wt.%. The Quaternary bauxite ore is characterized by variable concentrations of REEs (100.59–867.73 ppm, average of 403.69 ppm), LREEs (90.86–798.33 ppm, average of 344.63 ppm), and HREEs (10.09–294.01 ppm, average of 60.73 ppm). The Ce anomalies of the Quaternary bauxite ore are generally positive (0.22–3.19), while the Eu anomalies are generally negative (0.41–0.74). There are clear enrichments in REEs, LREEs, and HREEs in the Permian bauxite ore relative to the Quaternary bauxite ore (Fig. 4b). The REE, LREE, and HREE concentrations in the Permian bauxite ore are 296.62–4491.46 ppm (average of 1972.81 ppm), 254.41–3901.30 ppm (average of 1727.24 ppm), and 43.42–630.56 ppm (average of 261.58 ppm), respectively. The Ce and Eu anomalies vary from 0.44 to 1.45 and 0.49 to 0.57, respectively.

### 4.2. Mass change

The REE mass changes during the transition from Permian to Quaternary bauxite ore in the Longhe and Tianyang bauxite deposits were calculated using the immobile element method (MacLean and Kranidiotis, 1987; MacLean and Barrett, 1993). The changes in the mobile element components are calculated against an immobile element, Ti in the following example (MacLean et al., 1997). An enrichment factor (EF) is first calculated for each sample:

$$EF = Ti_{(\text{Permian bauxite ore})}/Ti_{(\text{Quaternary bauxite ore})} \quad (1)$$

and reconstituted compositions (RC) are computed for each rock component:

$$RC = EF \times (\text{abundance of an element}). \quad (2)$$

**Table 1**
Major and rare earth element compositions of bauxite samples from the Longhe and Tianyang bauxite deposits.

| Element | LQ-1 | LQ-2 | LQ-3 | LQ-4 | LQ-5 | LQ-6 | LQ-7 | LQ-8 | LP-1 | LP-2 | LP-3 |
|---|---|---|---|---|---|---|---|---|---|---|---|
| $SiO_2$ | 7.37 | 9.96 | 17.65 | 1.12 | 1.89 | 0.71 | 0.71 | 1.93 | 7.73 | 7.80 | 9.82 |
| $Al_2O_3$ | 44.95 | 38.13 | 39.09 | 51.80 | 42.20 | 51.97 | 53.58 | 44.82 | 57.42 | 51.24 | 49.40 |
| $Fe_2O_3$ | 26.63 | 33.57 | 28.07 | 30.77 | 33.79 | 28.08 | 25.44 | 31.42 | 7.88 | 9.43 | 16.98 |
| FeO | 0.52 | 0.15 | 0.13 | 0.12 | 0.12 | 0.25 | 0.12 | 0.24 | 9.53 | 12.85 | 5.30 |
| MgO | 0.13 | 0.11 | 0.11 | 0.08 | 0.10 | 0.07 | 0.09 | 0.12 | 0.66 | 0.29 | 0.14 |
| CaO | 0.08 | 0.05 | 0.06 | 0.05 | 0.05 | 0.07 | 0.06 | 0.07 | 0.08 | 0.21 | 0.07 |
| $Na_2O$ | 0.02 | 0.11 | 0.08 | 0.06 | 0.05 | 0.02 | 0.04 | 0.05 | 0.03 | 0.02 | 0.02 |
| $K_2O$ | 0.07 | 0.01 | 0.01 | 0.04 | 0.01 | 0.01 | 0.04 | 0.05 | 0.01 | 0.01 | 0.01 |
| MnO | 0.01 | 0.02 | 0.01 | 0.02 | 0.03 | 0.02 | 0.03 | 0.05 | 0.02 | 0.03 | 0.02 |
| $P_2O_5$ | 0.07 | 0.06 | 0.17 | 0.06 | 0.14 | 0.06 | 0.07 | 0.10 | 0.04 | 0.04 | 0.04 |
| $TiO_2$ | 4.96 | 3.44 | 2.07 | 3.94 | 5.46 | 4.51 | 4.35 | 5.07 | 2.45 | 4.17 | 3.50 |
| LOI | 15.61 | 14.38 | 12.41 | 11.81 | 15.58 | 14.58 | 15.19 | 15.65 | 13.79 | 13.73 | 14.30 |
| Total | 100.40 | 100.00 | 99.90 | 99.90 | 99.40 | 100.40 | 99.70 | 99.60 | 99.60 | 99.80 | 99.60 |
| La | 75.00 | 70.00 | 245.00 | 17.00 | 158.00 | 19.00 | 57.00 | 124.00 | 179.00 | 73.00 | 75.00 |
| Ce | 178.00 | 190.00 | 256.00 | 57.00 | 233.00 | 74.00 | 53.00 | 212.00 | 414.00 | 819.00 | 236.00 |
| Pr | 10.80 | 14.90 | 39.80 | 3.40 | 22.50 | 3.80 | 5.10 | 15.00 | 43.60 | 20.00 | 18.60 |
| Nd | 34.10 | 57.20 | 137.20 | 13.60 | 70.00 | 18.30 | 15.00 | 39.70 | 160.90 | 68.50 | 65.40 |
| Sm | 9.90 | 12.70 | 27.10 | 5.80 | 17.70 | 6.60 | 2.90 | 6.00 | 31.80 | 13.90 | 14.50 |
| Eu | 2.14 | 2.22 | 4.12 | 1.34 | 3.97 | 1.34 | 0.66 | 1.40 | 4.90 | 2.11 | 2.13 |
| Gd | 9.62 | 11.26 | 26.74 | 8.04 | 18.89 | 7.53 | 4.10 | 6.47 | 25.78 | 7.93 | 11.94 |
| Tb | 2.17 | 2.22 | 4.39 | 2.09 | 3.92 | 2.00 | 1.42 | 1.94 | 4.68 | 1.92 | 2.85 |
| Dy | 13.50 | 13.50 | 23.70 | 14.30 | 24.10 | 13.50 | 13.80 | 14.50 | 27.20 | 11.30 | 18.70 |
| Ho | 2.61 | 2.67 | 4.46 | 2.98 | 4.88 | 2.87 | 3.68 | 3.35 | 5.67 | 2.00 | 3.76 |
| Er | 7.93 | 8.12 | 12.97 | 9.43 | 14.20 | 8.93 | 12.77 | 10.14 | 17.70 | 5.74 | 11.77 |
| Tm | 1.38 | 1.53 | 2.18 | 1.96 | 2.68 | 1.67 | 2.36 | 1.89 | 3.28 | 1.11 | 2.24 |
| Yb | 8.90 | 10.10 | 13.50 | 13.10 | 17.30 | 11.90 | 14.20 | 12.00 | 20.20 | 7.60 | 14.60 |
| Lu | 1.28 | 1.48 | 2.02 | 1.94 | 2.48 | 1.64 | 2.20 | 1.72 | 2.94 | 1.12 | 2.20 |
| REE | 357.33 | 397.90 | 799.18 | 151.98 | 593.62 | 173.08 | 188.19 | 450.11 | 941.65 | 1035.23 | 479.69 |
| LREE | 309.94 | 347.02 | 709.22 | 98.14 | 505.17 | 123.04 | 133.66 | 398.10 | 834.20 | 996.51 | 411.63 |
| HREE | 47.39 | 50.88 | 89.96 | 53.84 | 88.45 | 50.04 | 54.53 | 52.01 | 107.45 | 38.72 | 68.06 |
| LREE/HREE | 6.54 | 6.82 | 7.88 | 1.82 | 5.71 | 2.46 | 2.45 | 7.65 | 7.76 | 25.74 | 6.05 |
| $(La/Yb)_N$ | 6.04 | 4.97 | 13.02 | 0.93 | 6.55 | 1.15 | 2.88 | 7.41 | 6.36 | 6.89 | 3.68 |
| $(La/Sm)_N$ | 4.89 | 3.56 | 5.84 | 1.89 | 5.76 | 1.86 | 12.69 | 13.34 | 3.63 | 3.39 | 3.34 |
| $(Gd/Lu)_N$ | 0.93 | 0.94 | 1.64 | 0.51 | 0.94 | 0.57 | 0.23 | 0.46 | 1.08 | 0.88 | 0.67 |

*(continued on next page)*

**Table 1** (*continued*)

| Element | LQ-1 | LQ-2 | LQ-3 | LQ-4 | LQ-5 | LQ-6 | LQ-7 | LQ-8 | LP-1 | LP-2 | LP-3 |
|---|---|---|---|---|---|---|---|---|---|---|---|
| Eu/Eu* | 0.66 | 0.56 | 0.46 | 0.60 | 0.66 | 0.58 | 0.58 | 0.68 | 0.51 | 0.56 | 0.48 |
| Ce/Ce* | 1.35 | 1.37 | 0.58 | 1.73 | 0.84 | 2.01 | 0.59 | 1.02 | 1.11 | 5.16 | 1.51 |

| Element | TQ-1 | TQ-2 | TQ-3 | TQ-4 | TQ-5 | TQ-6 | TQ-7 | TQ-8 | TQ-9 | TQ-10 | TQ-11 | TQ-12 | TQ-13 | TQ-14 | TQ-15 | TQ-16 | TQ-17 | TP-1 | TP-2 | TP-3 | TP-4 |
|---|---|---|---|---|---|---|---|---|---|---|---|---|---|---|---|---|---|---|---|---|---|
| $SiO_2$ | 1.16 | 1.33 | 12.82 | 6.81 | 9.09 | 2.11 | 5.44 | 11.16 | 15.70 | 0.95 | 6.36 | 6.12 | 13.85 | 1.44 | 0.29 | 7.77 | 12.78 | 19.77 | 12.98 | 11.00 | 6.63 |
| $Al_2O_3$ | 71.86 | 73.98 | 62.74 | 50.56 | 46.72 | 75.94 | 64.32 | 43.54 | 46.79 | 75.76 | 45.69 | 54.13 | 49.27 | 75.75 | 75.33 | 42.25 | 27.15 | 34.12 | 38.30 | 42.71 | 59.05 |
| $Fe_2O_3$ | 8.21 | 4.13 | 4.89 | 19.32 | 24.97 | 1.79 | 8.55 | 17.35 | 18.62 | 2.57 | 32.85 | 16.41 | 18.49 | 1.21 | 1.94 | 27.80 | 42.16 | 9.48 | 7.27 | 6.80 | 5.15 |
| FeO | 0.12 | 0.08 | 0.16 | 3.84 | 0.23 | 0.16 | 0.57 | 9.35 | 0.35 | 0.15 | 0.11 | 2.22 | 0.19 | 0.23 | 0.23 | 4.10 | 0.23 | 18.89 | 21.36 | 17.00 | 9.32 |
| MgO | 0.00 | 0.00 | 0.32 | 0.00 | 0.00 | 0.00 | 0.00 | 0.32 | 0.00 | 0.00 | 0.00 | 0.00 | 0.00 | 0.00 | 0.00 | 0.13 | 0.00 | 1.10 | 0.70 | 0.56 | 0.80 |
| CaO | 0.00 | 0.00 | 0.24 | 0.03 | 0.00 | 0.00 | 0.00 | 0.00 | 0.00 | 0.00 | 0.00 | 0.00 | 0.00 | 0.00 | 0.00 | 0.00 | 0.08 | 0.05 | 0.00 | 0.01 | 0.00 |
| $Na_2O$ | 0.13 | 0.00 | 0.68 | 0.00 | 0.00 | 0.03 | 0.09 | 0.00 | 0.15 | 0.00 | 0.00 | 0.00 | 0.00 | 0.01 | 0.00 | 0.00 | 0.26 | 0.66 | 0.14 | 1.10 | 0.00 |
| $K_2O$ | 0.04 | 0.01 | 0.50 | 0.01 | 0.02 | 0.06 | 0.27 | 0.01 | 0.02 | 0.00 | 0.00 | 0.00 | 0.00 | 0.03 | 0.01 | 0.00 | 1.33 | 0.79 | 0.01 | 0.04 | 0.01 |
| MnO | 0.00 | 0.00 | 0.36 | 0.11 | 0.00 | 0.00 | 0.03 | 0.02 | 0.01 | 0.00 | 0.00 | 0.00 | 0.01 | 0.00 | 0.00 | 0.02 | 0.01 | 0.06 | 0.04 | 0.04 | 0.02 |
| $P_2O_5$ | 0.04 | 0.05 | 0.08 | 0.15 | 0.05 | 0.15 | 0.05 | 0.05 | 0.06 | 0.03 | 0.02 | 0.08 | 0.16 | 0.07 | 0.07 | 0.08 | 0.11 | 0.02 | 0.04 | 0.06 | 0.03 |
| $TiO_2$ | 3.76 | 4.73 | 2.76 | 4.41 | 4.14 | 4.71 | 6.86 | 4.77 | 5.76 | 5.74 | 3.76 | 6.05 | 4.60 | 4.55 | 5.53 | 4.13 | 4.96 | 4.18 | 3.86 | 4.17 | 4.21 |
| LOI | 14.73 | 15.04 | 13.73 | 14.47 | 14.53 | 14.62 | 13.28 | 13.66 | 11.73 | 14.52 | 10.94 | 14.45 | 13.29 | 15.93 | 16.03 | 13.85 | 10.46 | 10.76 | 15.18 | 16.16 | 14.65 |
| Total | 100.06 | 99.35 | 99.28 | 99.71 | 99.75 | 99.57 | 99.46 | 100.23 | 99.18 | 99.73 | 99.73 | 99.46 | 99.86 | 99.23 | 99.42 | 100.14 | 99.53 | 99.86 | 99.88 | 99.65 | 99.86 |
| La | 22.00 | 51.00 | 141.00 | 87.00 | 79.00 | 262.00 | 54.00 | 124.00 | 114.00 | 23.00 | 18.00 | 393.00 | 42.00 | 20.00 | 16.00 | 36.00 | 92.00 | 157.00 | 299.00 | 1006.00 | 52.00 |
| Ce | 67.00 | 143.00 | 563.00 | 316.00 | 204.00 | 90.00 | 243.00 | 218.00 | 270.00 | 84.00 | 60.00 | 223.00 | 126.00 | 122.00 | 89.00 | 244.00 | 155.00 | 446.00 | 940.00 | 1035.00 | 148.00 |
| Pr | 4.70 | 11.00 | 19.00 | 15.70 | 13.90 | 21.20 | 11.20 | 17.00 | 12.90 | 2.80 | 2.70 | 38.70 | 6.50 | 5.50 | 3.50 | 9.30 | 22.20 | 47.00 | 106.90 | 321.90 | 10.80 |
| Nd | 17.00 | 36.00 | 62.00 | 49.00 | 47.00 | 70.00 | 37.00 | 41.00 | 33.00 | 8.00 | 8.00 | 86.00 | 23.00 | 23.00 | 15.00 | 35.00 | 85.00 | 181.00 | 420.00 | 1254.00 | 35.00 |
| Sm | 4.00 | 7.90 | 11.20 | 10.10 | 12.10 | 13.60 | 9.60 | 6.80 | 6.00 | 3.00 | 1.80 | 9.90 | 7.40 | 6.20 | 5.90 | 9.70 | 20.60 | 37.50 | 96.40 | 244.00 | 7.40 |
| Eu | 0.79 | 1.22 | 2.13 | 1.84 | 2.02 | 3.09 | 2.14 | 1.40 | 1.19 | 0.81 | 0.36 | 1.64 | 1.73 | 1.19 | 1.47 | 2.19 | 3.95 | 6.66 | 15.77 | 40.40 | 1.21 |
| Gd | 4.50 | 6.97 | 14.17 | 8.56 | 11.02 | 35.02 | 9.88 | 8.13 | 5.67 | 5.03 | 1.86 | 10.37 | 7.95 | 5.73 | 6.10 | 9.26 | 17.85 | 32.03 | 79.01 | 187.00 | 7.47 |
| Tb | 1.23 | 1.65 | 2.49 | 1.54 | 2.17 | 10.81 | 2.27 | 2.70 | 0.94 | 1.49 | 0.41 | 2.54 | 1.77 | 1.21 | 1.46 | 1.99 | 3.31 | 5.34 | 14.09 | 32.15 | 1.67 |
| Dy | 9.90 | 11.80 | 18.40 | 9.70 | 13.40 | 97.50 | 15.60 | 22.40 | 5.90 | 12.20 | 2.70 | 19.80 | 12.50 | 8.00 | 11.20 | 13.30 | 17.70 | 27.80 | 74.70 | 174.90 | 11.70 |
| Ho | 2.19 | 2.39 | 4.19 | 1.81 | 2.55 | 23.60 | 3.03 | 4.36 | 1.12 | 2.67 | 0.53 | 4.29 | 2.52 | 1.53 | 2.35 | 2.64 | 2.96 | 4.59 | 12.17 | 29.61 | 2.46 |
| Er | 6.81 | 7.27 | 12.65 | 4.88 | 7.29 | 64.72 | 8.72 | 12.96 | 3.34 | 8.03 | 1.58 | 12.38 | 7.50 | 4.48 | 7.22 | 7.79 | 7.48 | 11.65 | 31.48 | 77.10 | 7.37 |
| Tm | 1.32 | 1.44 | 2.22 | 0.78 | 1.34 | 9.05 | 1.62 | 2.53 | 0.63 | 1.49 | 0.31 | 2.05 | 1.45 | 0.85 | 1.38 | 1.52 | 1.22 | 1.76 | 5.39 | 11.88 | 1.38 |
| Yb | 8.70 | 9.57 | 13.28 | 4.68 | 8.54 | 43.79 | 10.55 | 16.98 | 4.36 | 9.39 | 2.04 | 12.13 | 9.48 | 5.79 | 9.19 | 9.99 | 7.24 | 9.98 | 33.66 | 67.78 | 8.84 |
| Lu | 1.27 | 1.45 | 2.00 | 0.63 | 1.26 | 6.43 | 1.53 | 2.48 | 0.64 | 1.34 | 0.30 | 1.78 | 1.42 | 0.85 | 1.34 | 1.50 | 1.03 | 1.36 | 4.91 | 9.74 | 1.32 |
| REE | 151.41 | 292.66 | 867.73 | 512.22 | 405.59 | 750.81 | 410.14 | 480.74 | 459.69 | 163.25 | 100.59 | 817.58 | 251.22 | 206.33 | 171.11 | 384.18 | 437.54 | 969.67 | 2133.48 | 4491.46 | 296.62 |
| LREE | 115.49 | 250.12 | 798.33 | 479.64 | 358.02 | 459.89 | 356.94 | 408.20 | 437.09 | 121.61 | 90.86 | 752.24 | 206.63 | 177.89 | 130.87 | 336.19 | 378.75 | 875.16 | 1878.07 | 3901.30 | 254.41 |
| HREE | 35.92 | 43.76 | 71.53 | 34.42 | 49.59 | 294.01 | 55.34 | 73.94 | 23.79 | 42.45 | 10.09 | 66.98 | 46.32 | 29.63 | 41.71 | 50.18 | 62.74 | 101.17 | 271.18 | 630.56 | 43.42 |
| LREE/HREE | 3.22 | 5.72 | 11.16 | 13.93 | 7.22 | 1.56 | 6.45 | 5.52 | 18.37 | 2.86 | 9.00 | 11.23 | 4.46 | 6.00 | 3.14 | 6.70 | 6.04 | 8.65 | 6.93 | 6.19 | 5.86 |
| $(La/Yb)_N$ | 1.81 | 3.82 | 7.62 | 13.33 | 6.64 | 4.29 | 3.67 | 5.24 | 18.76 | 1.76 | 6.33 | 23.24 | 3.18 | 2.48 | 1.25 | 2.58 | 9.11 | 11.28 | 6.37 | 10.65 | 4.22 |
| $(La/Sm)_N$ | 3.55 | 4.17 | 8.13 | 5.56 | 4.21 | 12.44 | 3.63 | 11.77 | 12.27 | 4.95 | 6.46 | 25.63 | 3.66 | 2.08 | 1.75 | 2.40 | 2.88 | 2.70 | 2.00 | 2.66 | 4.54 |
| $(Gd/Lu)_N$ | 0.44 | 0.59 | 0.88 | 1.68 | 1.08 | 0.67 | 0.80 | 0.41 | 1.10 | 0.46 | 0.77 | 0.72 | 0.69 | 0.83 | 0.56 | 0.76 | 2.14 | 2.91 | 1.99 | 2.37 | 0.70 |
| Eu/Eu* | 0.57 | 0.49 | 0.52 | 0.59 | 0.52 | 0.41 | 0.67 | 0.57 | 0.61 | 0.63 | 0.60 | 0.49 | 0.69 | 0.60 | 0.74 | 0.70 | 0.61 | 0.57 | 0.54 | 0.56 | 0.49 |
| Ce/Ce* | 1.54 | 1.41 | 2.31 | 1.94 | 1.39 | 0.22 | 2.30 | 1.01 | 1.43 | 2.17 | 1.88 | 0.35 | 1.68 | 2.80 | 2.79 | 3.19 | 0.81 | 1.26 | 1.29 | 0.44 | 1.45 |

$Eu/Eu^* = (2Eu/Eu_{ch}) / (Sm/Sm_{ch} + Gd/Gd_{ch})$; $Ce/Ce^* = (2Ce/Ce_{ch}) / (La/La_{ch} + Pr/Pr_{ch})$; $(La/Yb)_N = (La/La_{ch}) / (Yb/Yb_{ch})$; $(La/Sm)_N = (La/La_{ch}) / (Sm/Sm_{ch})$, and $(Gd/Lu)_N = (Gd/Gd_{ch}) / (Lu/Lu_{ch})$. Samples with number from LQ-1 to LQ-8 represent Longhe Quaternary bauxite ores, LP-1 to LP-3 are Longhe Permian bauxite ores, TQ-1 to TQ-17 are Tianyang Quaternary bauxite ores, and TP-1 to TP-4 represent Tianyang Permian bauxite ores.

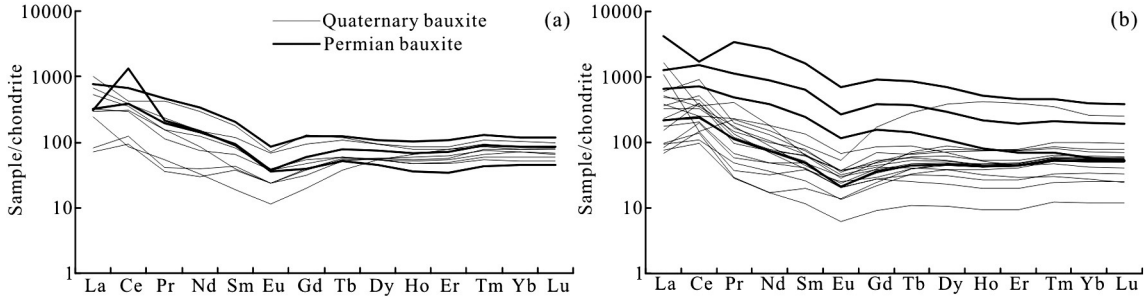


**Fig. 4.** Chondrite-normalized REE patterns of Permian and Quaternary bauxite ores in the (a) Longhe bauxite deposit; and (b) Tianyang bauxite deposit.

The mass changes are calculated as follows:

$$\text{Mass change} = \text{RC} - \text{precursor}. \quad (3)$$

The calculated mass changes of the REEs, illustrated in Fig. 5, show that each of the REEs in the Longhe and Tianyang bauxite deposits have undergone differing degrees of depletion. However, in general, the LREEs show a greater depletion than the HREEs. The elements that show the greatest calculated depletion are Ce, Nd, La, and Pr in the Longhe bauxite deposit (Fig. 5a), and Ce, Nd, La, Pr, Sm, Gd, and Dy in the Tianyang bauxite deposit (Fig. 5b).

## 5. Mineralogy

### 5.1. Mineral compositions

The mineral species and their occurrences in the bauxite ore were analyzed by XRD and EPMA (Figs. 6 and 7).

Based on the results of Wang et al. (2010) and our analyses, we find that diaspore, amesite, chamosite, and anatase are the main minerals in the Permian Xinxu bauxite ore, along with minor hematite, goethite, rutile, parisite, bastnäsite, and zircon. Diaspore and anatase are dominant in the Quaternary Xinxu bauxite ore, along with minor amesite, chamosite, goethite, rutile, parisite, and churchite.

In the Longhe bauxite deposit, diaspore, amesite, chamosite, anatase, and hematite are the main minerals in the Permian bauxite mineral assemblage, along with minor goethite, rutile, bastnäsite, and rhabdophane. The Quaternary bauxite mineral assemblage is dominated by diaspore, hematite, goethite, and anatase, along with minor amesite, quartz, and rutile.

In the Tianyang bauxite deposit, amesite, diaspore, illite, chamosite, and anatase are the main minerals in the Permian bauxite mineral assemblage, along with minor rutile, pyrite, cerianite, Mn–Al hydroxide, Al-goethite, and chloride. The Tianyang Quaternary bauxite mineral assemblage is dominated by diaspore, anatase, and rutile.

### 5.2. Occurrence and chemical compositions of REE minerals

#### 5.2.1. REE fluorocarbonates

In karstic bauxite deposits worldwide, rare earth fluorocarbonates are widely developed and are dominated by bastnäsite and parisite. Bastnäsite has the formula $REECO_3F$, and parisite is $CaREE_2(CO_3)_3F_2$. The $Ca^{2+}$ in the parisite lattice can be replaced by $REE^{3+}$ in karstic bauxite (Mongelli, 1997; Wang et al., 2010). In this study, the fine grain sizes of the rare earth fluorocarbonates hindered their separation from the bauxite ore for individual analysis using XRD. Therefore, chemical compositions obtained by EPMA were used to distinguish the species of REE minerals. According to our EPMA analyses, both bastnäsite and parisite are present in both the Quaternary and Permian bauxite ore (Tables 2 and 3). In addition, we note the REE concentrations in the rare earth fluorocarbonates show wide variations (Tables 2 and 3).

The Permian Xinxu bauxite ore contains pervasive rare earth fluorocarbonates, identified in both the matrix and ooids (Fig. 7a). These fluorocarbonates occur mainly in association with chamosite and diaspore, but also in bands of internal zoning within ooids (Fig. 7a). EPMA results suggest that these fluorocarbonates are bastnäsites, which contain low CaO contents (0.93–1.36 wt.%). The bastnäsite has a high concentration of $Ce_2O_3$ (46.03–52.91 wt.%) and also contains $Nd_2O_3$ (5.45–6.67 wt.%), $La_2O_3$ (3.57–5.85 wt.%), $Pr_2O_3$ (1.45–4.68 wt.%), $Y_2O_3$ (below the detection limit [b.d.l.] to 0.80 wt.%), $Sm_2O_3$ (b.d.l. to 2.74 wt.%), $Yb_2O_3$ (b.d.l. to 0.84 wt.%), $Gd_2O_3$ (b.d.l. to 1.80 wt.%), $Tm_2O_3$ (b.d.l. to 2.02 wt.%), $Er_2O_3$ (b.d.l. to 0.53 wt.%), and $Eu_2O_3$ (b.d.l. to 0.37 wt.%). This indicates that the bastnäsite in the Permian Xinxu bauxite ore is of the bastnäsite-(Ce) type. In addition to abundant REEs, the bastnäsite-(Ce) contains $Al_2O_3$ (0.95–3.49 wt.%), $SiO_2$ (0.83–1.72 wt.%), $TiO_2$ (b.d.l. to 1.09 wt.%), and FeO (b.d.l. to 4.00 wt.%). These major

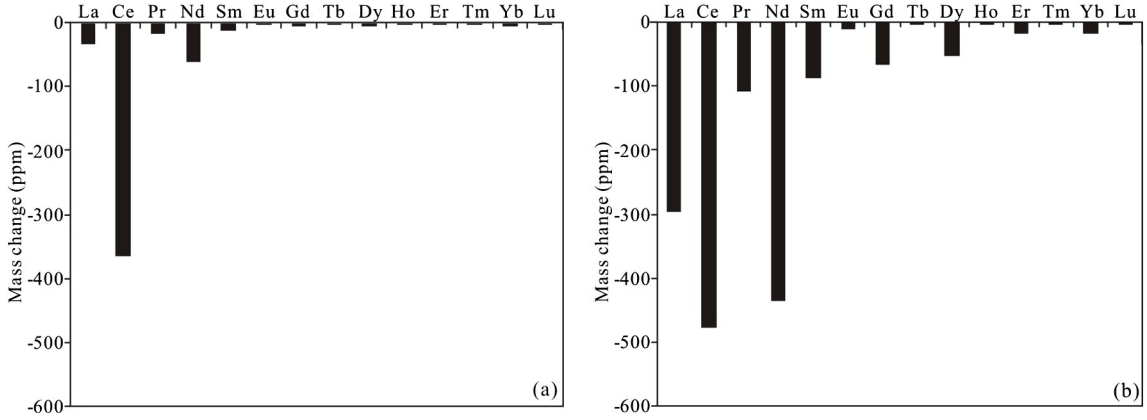


**Fig. 5.** Mass changes of rare-earth elements during the transformation from Permian to Quaternary bauxite ore, in the (a) Longhe bauxite deposit; and (b) Tianyang bauxite deposit. Ti was used as the immobile element during calculations.

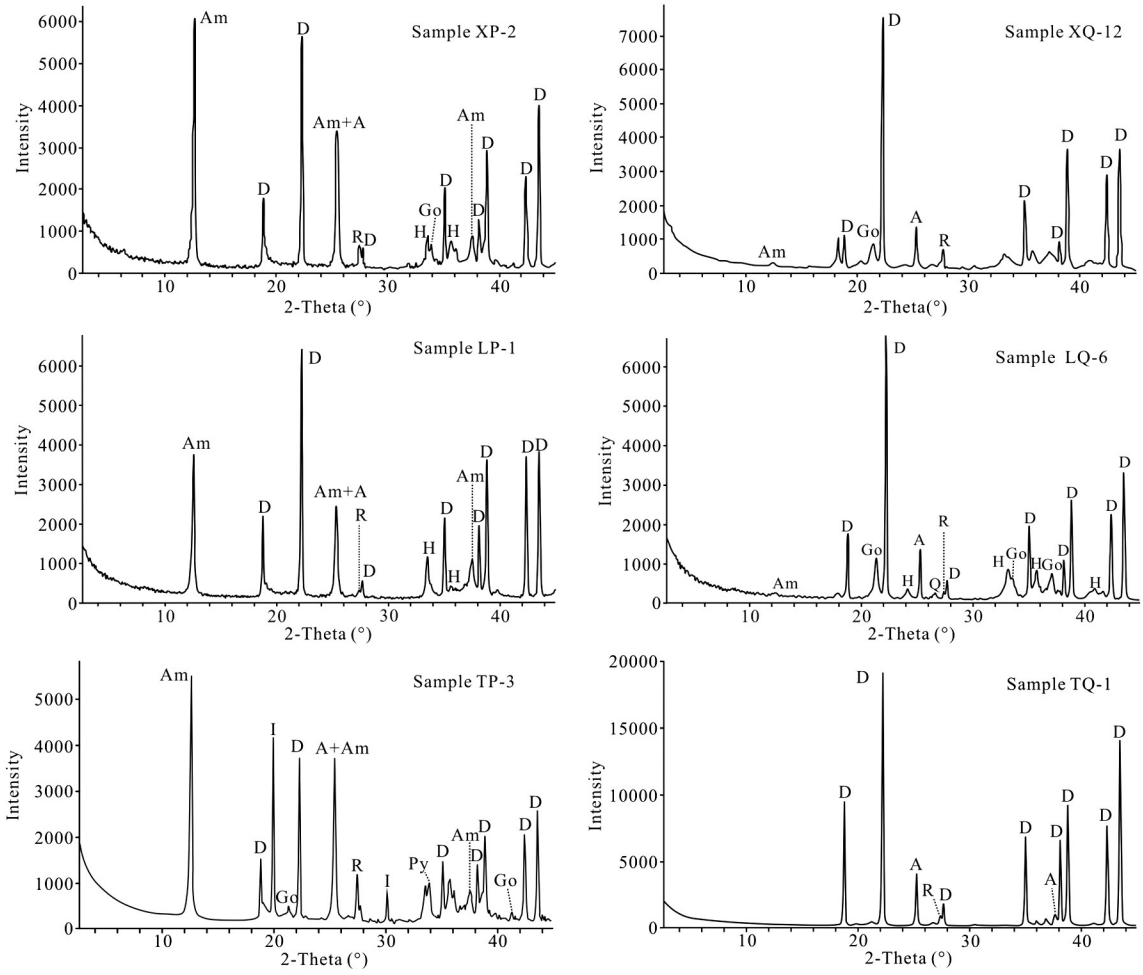


**Fig. 6.** XRD spectra showing mineral components in typical bauxite ores from the Xinxu (upper spectra), Longhe (middle spectra), and Tianyang (lower spectra) bauxite deposits. (D, diaspore; Am, amesite; Go, goethite; H, hematite; R, rutile; I, illite; A, anatase; Py, pyrite; Q, quartz).

elements are primarily related to the presence of minor diaspore, chamosite, and anatase inclusions, or were affected by surrounding minerals during the analysis.

In the Quaternary Xinxu bauxite ore, rare earth fluorocarbonates are scarce, occurring as single crystals distributed throughout the diaspore-dominated matrix (Fig. 7b). The rare earth fluorocarbonate is identified as parisite based on the EPMA analysis results and shows partial dissolution of crystal surfaces (Table 2; Fig. 7b). The parisite in the Quaternary Xinxu bauxite ore is characterized by high contents of $REE_2O_3$ (67.78–74.78 wt.%) and low contents of CaO (b.d.l. to 1.44 wt.%), indicating pervasive replacement of $Ca^{2+}$ by $REE^{3+}$. The REEs in the parisite include $Nd_2O_3$ (23.19–30.12 wt.%), $Ce_2O_3$ (10.75–17.85 wt.%), $Pr_2O_3$ (6.73–11.92 wt.%), $Sm_2O_3$ (6.51–8.29 wt.%), $La_2O_3$ (2.24–2.60 wt.%), $Y_2O_3$ (1.97–3.65 wt.%), $Gd_2O_3$ (5.06–5.19 wt.%), $Er_2O_3$ (b.d.l. to 0.92 wt.%), $Yb_2O_3$ (b.d.l. to 0.48 wt.%), $Dy_2O_3$ (b.d.l. to 1.59 wt.%), $Tb_2O_3$ (b.d.l. to 1.31 wt.%), and $Eu_2O_3$ (0.61–1.58 wt.%) (Table 2). These results suggest that the parisite in the Quaternary bauxite ore is of the parisite-(Nd) type. The parisite-(Nd) also contains $Al_2O_3$ (0.88–1.31 wt.%), $SiO_2$ (0.19–0.61 wt.%), and FeO (b.d.l. to 0.05 wt.%).

The Permian Longhe bauxite ore is rich in rare earth fluorocarbonates, which occur in both the matrix and in ooids (Fig. 7c and d). Some grains were selected for compositional analysis, and the results are listed in Table 3. The rare earth fluorocarbonates in the Longhe Permian bauxite ore are bastnäsite that has higher $CaO_2$ (2.14–2.64 wt.%) and lower $REE_2O_3$ (51.92–63.96 wt.%) than the Permian Xinxu bauxite ore. The REEs in the bastnäsite include $Ce_2O_3$ (23.13–27.63 wt.%), $Nd_2O_3$ (8.19–10.41 wt.%), $Pr_2O_3$ (2.79–7.89 wt.%), $Sm_2O_3$ (1.06–3.17 wt.%), $La_2O_3$ (5.46–8.98 wt.%), $Y_2O_3$ (0.31–1.16 wt.%), $Gd_2O_3$ (1.59–4.15 wt.%), $Eu_2O_3$ (b.d.l. to 1.11 wt.%), $Er_2O_3$ (b.d.l. to 0.67 wt.%), $Yb_2O_3$ (b.d.l. to 0.78 wt.%), $Dy_2O_3$ (b.d.l. to 2.08 wt.%), $Tb_2O_3$ (b.d.l. to 1.31 wt.%), $Tm_2O_3$ (b.d.l. to 1.76 wt.%), and $Ho_2O_3$ (b.d.l. to 1.38 wt.%). This indicates that the bastnäsite is of the bastnäsite-(Ce) type. Other elements, including $Al_2O_3$ (b.d.l. to 3.11 wt.%), $SiO_2$ (0.30–2.10 wt.%), and FeO (5.76–12.19 wt.%), were also detected in the bastnäsite.

### 5.2.2. Rhabdophane

Rhabdophane, with the chemical formula $(REE)PO_4 \cdot nH_2O$, was only detected in the Longhe Permian bauxite ore. Rhabdophane grains occurred mainly along the margin of a goethite vein that cuts the matrix of the Permian bauxite ore (Fig. 7e and f). As the rhabdophane crystals are too small for individual analysis, precise chemical data could not be obtained; however, some EPMA data are presented in Table 3. The rhabdophane contain $Fe_2O_3$ (2.90–16.94 wt.%), $Al_2O_3$ (2.96–8.39 wt.%), $SiO_2$ (0.31–3.32 wt.%), along with minor MgO and $TiO_2$. However, it is likely that surrounding minerals such as goethite, chamosite, and diaspore were also sampled during the analysis. The $P_2O_5$ concentrations in the analyzed grains range from 16.75 to 24.46 wt.%. Nearly all the REEs were identified in the rhabdophane grains, including $Ce_2O_3$ (23.48–25.63 wt.%), $Nd_2O_3$ (7.14–10.14 wt.%), $La_2O_3$ (7.30–8.47 wt.%), $Pr_2O_3$ (2.58–4.59 wt.%), $Y_2O_3$ (0.45–2.80 wt.%), $Gd_2O_3$ (b.d.l. to 3.44 wt.%), $Sm_2O_3$ (b.d.l. to 2.14 wt.%), $Dy_2O_3$ (b.d.l. to 2.34 wt.%), $Ho_2O_3$ (b.d.l. to 2.43 wt.%), $Yb_2O_3$ (b.d.l. to 0.92 wt.%), $Tm_2O_3$ (b.d.l. to 2.77 wt.%), $Tb_2O_3$ (b.d.l. to 1.60 wt.%), and $Eu_2O_3$ (b.d.l. to 0.72 wt.%).

*5.2.3. Cerianite*

Cerianite, with the chemical formula $CeO_2$, was identified in one sample from the Tianyang Permian bauxite ore, and generally coexists with Mn–Al hydroxide and Al-goethite (Fig. 7g and h). The assemblage of cerianite, Mn–Al hydroxide, and Al-goethite occurs in a fracture cutting the Permian bauxite ore that is composed mainly of chamosite and diaspore. The Mn–Al hydroxide occurs in the center of the assemblage, as a vein, while the cerianite occurs at the boundary of Mn–Al hydroxide veins in association with Al-goethite veins (Fig. 7h). Crystalline chloride also occurs locally (Fig. 7h).

The chemical compositions of cerianite, Mn–Al hydroxide, and Al-goethite are listed in Table 4. The cerianite contains $CeO_2$ (74.47–84.87 wt.%), $Al_2O_3$ (1.74–3.05 wt.%), $SiO_2$ (1.76–2.68 wt.%), $Fe_2O_3$ (1.91–2.93 wt.%), CaO (0.17–0.57 wt.%), and MnO (b.d.l. to 1.83 wt.%), probably reflecting contamination by other micro-mineral inclusions during analysis. Minor $Y_2O_3$ were also identified (Table 4). The Mn–Al hydroxide is composed of MnO (45.04–47.34 wt.%), $Al_2O_3$ (22.08–23.58 wt.%), $Fe_2O_3$ (3.22–3.58 wt.%), and minor CaO, $SiO_2$, and MgO. The Al-goethite is dominated by $Fe_2O_3$ (59.18 wt.%), $Al_2O_3$ (15.52 wt.%), $SiO_2$ (3.41 wt.%), and minor MnO, $TiO_2$, CaO, and MgO.

## 6. Discussion

### 6.1. Genesis of REE minerals

*6.1.1. REE fluorocarbonates*

Limestone aquifers play a major role during karst bauxitization. These waters are generally close to equilibrium with calcite and have a near-neutral to slightly-alkaline pH (Appelo and Postma, 1993; Mongelli, 1997). At such pH levels, REE–carbonate complexes prevail (Johannesson et al., 1995, 1996).

In western Guangxi, the water conditions during the Permian bauxite ore-forming stage were alkaline and reducing (Liu et al., 2012). These conditions are favorable for the widespread development of REE–fluorocarbonates (Fig. 8a), as indicated by the extensive development of bastnäsite and parisite in various ore textures; e.g., in the matrix and in the cores and bands of internal zoning within ooids. It is generally accepted that the REEs were transported into the karstic environment mainly as adsorbed ions on the surfaces of clay particles or REE minerals, such as cerianite, in the upper part of the weathering profile (Bárdossy, 1982; Mongelli, 1997; Wang et al., 2010). The $Ce^{4+}$ in the cerianite was possibly transformed into $Ce^{3+}$ by the decrease in Eh inside the karstic depression (Mongelli, 1997; Liu et al., 2012). In their adsorbed form, the REEs were easily removed by percolating water and subsequently concentrated on the geochemical barrier of the footwall limestone, forming the REE–fluorocarbonates (Mongelli, 1997; Fig. 8a).

It is not uncommon for the chemical compositions of REE–fluorocarbonates to vary greatly within the same deposit. For example, bastnäsite-(Ce) in microveins of the Nagyharsány bauxite deposit has a $Ce_2O_3$ concentration of 21.5 wt.%, while the bastnäsite-(Ce) found within segregations of the same deposit contains 72.3 wt.% $Ce_2O_3$ (Maksimovic and Pantó, 1983), the Marmara bauxite deposit contains coexisting bastnäsite-(Ce) and bastnäsite-(La) minerals (Maksimovic and Pantó, 1996), and deposits containing hydroxylbastnäsite-(Nd) and hydroxylbastnäsite-(La) occur in Montenegro (Maksimovic and Pantó, 1996). The variations in REE contents in the authigenic REE minerals arise mainly from the initial REE concentrations in the original weathered material, and from the intensity of leaching of this material by percolating waters in a karstic environment (Maksimovic and Pantó, 1996). In the bauxite deposits of western Guangxi, bastnäsite-(Ce), parisite-(Nd), and parisite-(Ce) were formed only in the Permian karstic environment, which is characterized by universal alkaline and reducing conditions in the karstic depressions (Liu et al., 2012). Therefore, the variable REE contents of the REE–fluorocarbonates of this study are most likely related to the initial contents of REEs in the original weathered material.

*6.1.2. Rhabdophane*

In general, rhabdophane occurs in the lower section of lateritic profiles due to the increasing pH with depth (Murakami et al., 2001; Sanematsu et al., 2013; Berger et al., 2014). In lateritic profiles, rhabdophane is usually strongly or more rarely moderately depleted in Ce compared with concentrations in whole rocks in oxidized weathering profiles (Sawka et al., 1986; Banfield and Eggleton, 1989; Braun et al., 1998; Murakami et al., 2001; Berger et al., 2014). This is mainly due to the oxidation of $Ce^{3+}$ to $Ce^{4+}$ in the upper section of the weathered profile and the subsequent precipitation of cerianite under oxidizing conditions (Braun et al., 1990, 1993; Sanematsu et al., 2013). Previous studies have reported Ce-poor rhabdophane and cerianite ($Ce^{4+}O_2$) in the lower and upper sections of a lateritic profile, respectively (Mongelli, 1997; Sanematsu et al., 2013; Berger et al., 2014). Therefore, oxidizing weathering processes result in the precipitation of Ce-free or Ce-poor rhabdophane and cerianite, and Ce fractionation differs between rhabdophane and weathered rocks.

In contrast, rhabdophane grains in the Longhe Permian bauxite ore contain relatively large amounts Ce, Nd, La, Pr, and Y. Ce-rich rhabdophane has been identified in a 2.60–2.45 Ga paleosol developed on Archean granite near the Pronto mine, Canada, and is considered to relate to the anoxic atmosphere in the late Archean to early Proterozoic (Murakami et al., 2001). However, western Guangxi lacked such a favorable atmosphere after the formation of the Permian bauxite ore. The mode of occurrence of rhabdophane in the Longhe bauxite ore suggests that they formed during a period dominated by oxidizing and acidic conditions, like those during the Quaternary weathering stage as opposed to the reducing and alkaline conditions of the late Permian (Liu et al., 2012). Therefore, the anoxic atmosphere model does not explain the genesis of rhabdophane in the Longhe bauxite. In addition to rhabdophane, bastnäsite occurs in the analyzed sample (Fig. 7c), and both have similar REE compositions (Table 3). This result suggests that the REEs in rhabdophane originated from adjacent bastnäsite in the Permian bauxite ore.

During the Quaternary weathering, some amesite/chamosite and bastnäsite grains were dissolved, and ions (e.g., $Al^{3+}$, $Si^{4+}$, $Fe^{2+}$, and $REE^{3+}$) were released into solutions in fractures that cut the bauxite ore. The $REE^{3+}$-enriched solutions, together with P originating from the overlying laterite, experienced weakly oxidizing conditions in the fractures; consequently, $Ce^{3+}$ did not rapidly oxidize to $Ce^{4+}$. The Ce-rich rhabdophane probably formed under such conditions (Fig. 8c).

*6.1.3. Cerianite*

Cerianite is generally considered to precipitate in weathering profiles under the following conditions: variable pH from 5 to 6, Ce activity of $10^{-9}$ M, and Eh values of 0.38–0.61 V (Mongelli, 1997). In some cases, Ce-bearing Mn oxides and cerianite in association with Fe–Mn oxides can be identified in weathering profiles, as $Ce^{3+}$ is oxidized to $Ce^{4+}$ by Mn and Fe oxides (Bau, 1999; Ohta and Kawabe, 2001; Sanematsu et al., 2013).

In this study, the mode of occurrence of the cerianite suggests it formed during Quaternary weathering. The $Ce^{3+}$ could have originated from weathering of the laterite that overlies the Permian bauxite horizon, or from the dissolution of REE–fluorocarbonates in the Permian bauxite ore. We prefer the latter hypothesis, as $Ce^{3+}$ released from minerals in overlying strata would have been rapidly oxidized to $Ce^{4+}$. Instead, the $Ce^{3+}$ released from REE–fluorocarbonates was oxidized to $Ce^{4+}$ by the presence of Mn–Al and Fe hydroxides that formed along with cerianite in fractures within the Permian bauxite ore (Fig. 8d).

*6.1.4. Churchite*

Although churchite, $Y(PO_4)\cdot 2(H_2O)$, was not identified in this study, it has been reported in previous studies of Permian karstic bauxite deposits in south China (Liu, 1994; Wang et al., 2010). Churchite is commonly formed in acidic environments (pH = 0.5–3.0; Hukuo and Hikichi, 1979). Wang et al. (2010) suggested that churchite form at the same

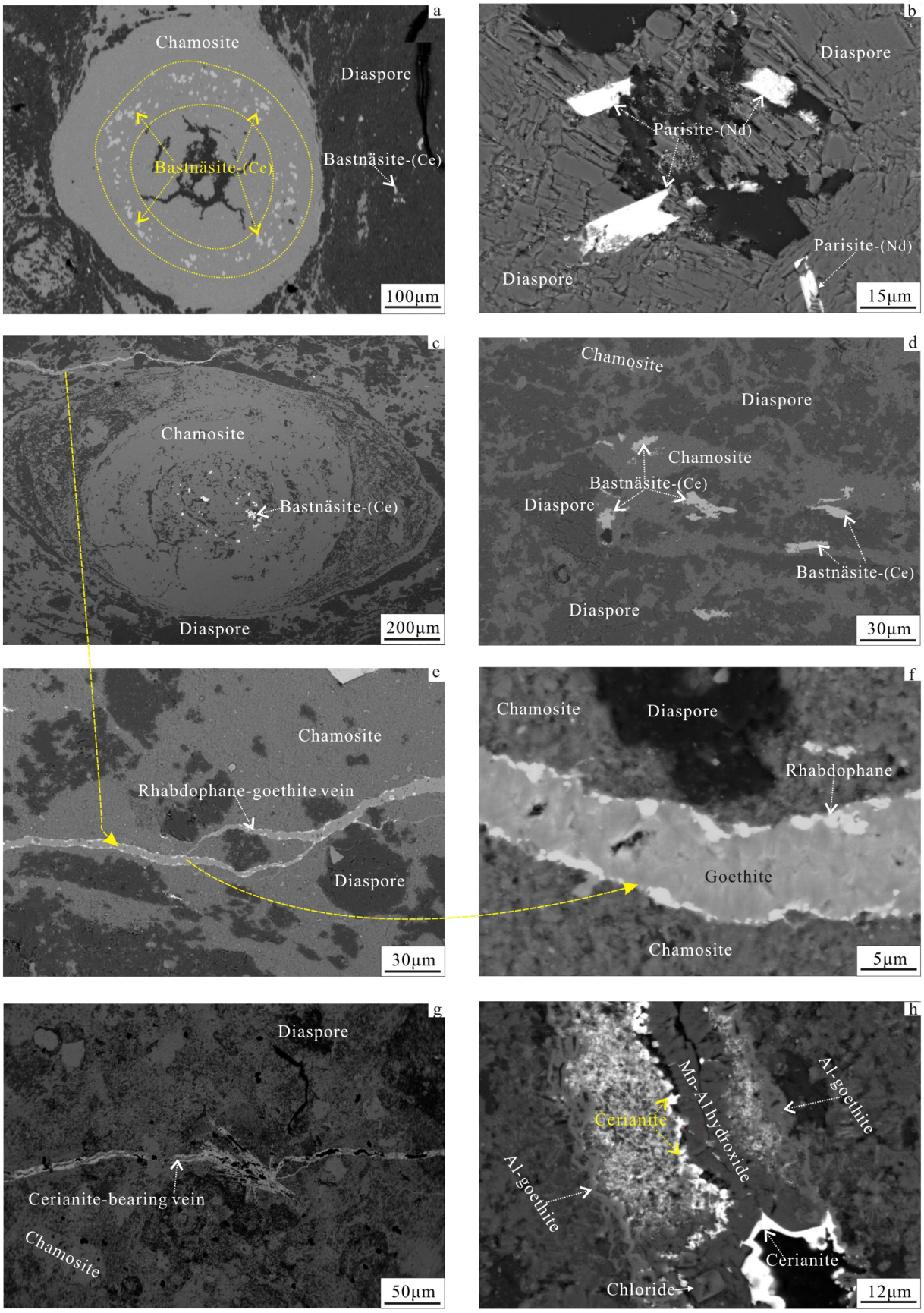

**Table 2**
Electron probe X-ray microanalyses (wt.%) of bastnäsite and parisite in samples XP-2 and XQ-12 from the Xinxu bauxite deposit.

| Sample | XP-2 | | | | | | XQ-12 | |
|---|---|---|---|---|---|---|---|---|
| Plot | Bastnäsite-(Ce) | | | | | | Parisite-(Nd) | |
| | Plot-1 | Plot-2 | Plot-3 | Plot-4 | Plot-5 | Plot-6 | Plot-7 | Plot-8 |
| F | 6.53 | 7.13 | 7.87 | 7.44 | 7.07 | 8.26 | 5.87 | 5.33 |
| MgO | b.d.l. | b.d.l. | b.d.l. | b.d.l. | 0.21 | b.d.l. | b.d.l. | b.d.l. |
| $Al_2O_3$ | 1.56 | 1.10 | 0.95 | 3.49 | 3.30 | 2.26 | 0.88 | 1.31 |
| $SiO_2$ | 1.40 | 1.10 | 1.22 | 1.72 | 0.83 | 1.24 | 0.61 | 0.19 |
| CaO | 1.16 | 1.36 | 1.33 | 0.93 | 1.22 | 1.18 | 1.44 | b.d.l. |
| $TiO_2$ | b.d.l. | 0.15 | 0.46 | 0.48 | b.d.l. | 1.09 | b.d.l. | b.d.l. |
| MnO | b.d.l. | b.d.l. | b.d.l. | b.d.l. | b.d.l. | b.d.l. | b.d.l. | 0.27 |
| FeO | b.d.l. | 1.40 | 1.85 | 4.00 | 2.83 | 3.29 | b.d.l. | 0.05 |
| $Y_2O_3$ | 0.75 | 0.80 | 0.50 | b.d.l. | 0.23 | 0.63 | 3.65 | 1.97 |
| $La_2O_3$ | 4.58 | 5.83 | 5.85 | 4.81 | 3.57 | 5.40 | 2.60 | 2.24 |
| $Ce_2O_3$ | 52.91 | 50.68 | 51.05 | 47.5 | 46.03 | 47.55 | 17.85 | 10.75 |
| $Pr_2O_3$ | 2.16 | 1.45 | 1.94 | 3.78 | 4.68 | 2.10 | 6.73 | 11.92 |
| $Nd_2O_3$ | 5.45 | 5.87 | 5.63 | 5.95 | 6.67 | 6.55 | 23.19 | 30.12 |
| $Sm_2O_3$ | 0.29 | 0.36 | 1.15 | 1.56 | 2.74 | b.d.l. | 6.51 | 8.29 |
| $Eu_2O_3$ | b.d.l. | b.d.l. | b.d.l. | b.d.l. | 0.37 | b.d.l. | 1.58 | 0.61 |
| $Gd_2O_3$ | 1.60 | 0.49 | b.d.l. | b.d.l. | 1.80 | 1.36 | 5.19 | 5.06 |
| $Tb_2O_3$ | b.d.l. | b.d.l. | b.d.l. | b.d.l. | b.d.l. | b.d.l. | b.d.l. | 1.31 |
| $Dy_2O_3$ | b.d.l. | b.d.l. | b.d.l. | b.d.l. | b.d.l. | b.d.l. | b.d.l. | 1.59 |
| $Er_2O_3$ | b.d.l. | b.d.l. | b.d.l. | b.d.l. | 0.46 | 0.53 | b.d.l. | 0.92 |
| $Tm_2O_3$ | b.d.l. | 0.87 | 2.02 | b.d.l. | b.d.l. | b.d.l. | b.d.l. | b.d.l. |
| $Yb_2O_3$ | 0.11 | 0.48 | 0.84 | 0.31 | b.d.l. | 0.62 | 0.48 | b.d.l. |
| Total | 71.98 | 71.95 | 74.78 | 74.53 | 75.38 | 73.81 | 70.71 | 76.9 |
| $REE_2O_3$ | 67.85 | 66.83 | 68.98 | 63.91 | 66.55 | 64.74 | 67.78 | 74.78 |
| $REE_2O_3$/CaO | 58.49 | 49.14 | 51.86 | 68.72 | 54.55 | 54.86 | 47.07 | b.d.l. |
| Atomic ratios calculated to | | | | | | | | |
| | (O, F) = 4 | | | | | | (O, F) = 11 | |
| REE[a] | 0.94 | 0.94 | 1.04 | 1.02 | 1.03 | 1.01 | 2.46 | 3.05 |
| Ca | 0.05 | 0.06 | 0.06 | 0.04 | 0.06 | 0.05 | 0.15 | 0.00 |
| F | 0.78 | 0.87 | 1.03 | 1.03 | 0.96 | 1.11 | 1.84 | 1.91 |
| C | 1.07 | 1.05 | 0.93 | 0.95 | 0.96 | 0.94 | 3.11 | 2.74 |

[a] REE represents the sum of the atomic ratios of all rare earth elements. To obtain more precise atomic ratios of REE, F, Ca, and C, the oxides $Al_2O_3$, $SiO_2$, FeO, and $TiO_2$ were distributed to $REE_2O_3$, CaO, and F according to their proportions. $CO_2$ used in the calculation was calculated to sum of 100%.

stage as parisite but at different depths in bauxitic soil. However, previous studies have found that the conditions of formation of Permian bauxite ore are typically reduced and alkaline (pH > 7) (Liu et al., 2010, 2012), which are not favorable for the precipitation of churchite. Therefore, we believe that churchite was most likely formed in the Permian weathering period under acidic and oxidizing conditions.

### 6.2. Genetic significance

#### 6.2.1. Implications for REE behavior

Although the REEs have similar chemical properties to each other, they experience inter-elemental fractionation during weathering (Mongelli, 1997). The weathered material can be enriched in LREEs and depleted in HREEs relative to the parent rock (Nesbitt, 1979; Duddy, 1980; Topp et al., 1984; Mongelli, 1997; Karadağ et al., 2009; Liu et al., 2013), and it can show positive Ce anomalies due to the $Ce^{3+} \rightarrow Ce^{4+}$ redox change (Rankin and Childs, 1976; Steinberg and Courtois, 1976; Marsh, 1991).

The mass changes that occurred during the transition from Permian to Quaternary bauxite in the Longhe and Tianyang bauxite deposits indicate that nearly all the REEs in this study are depleted, especially the LREEs (e.g., Ce, Nd, La, Pr, Sm, Gd, and Dy) in the Tianyang bauxite deposit and Ce, Nd, La, and Pr in the Longhe bauxite deposit. This result differs from the traditional concept that enrichment in LREEs and depletion in HREEs occur during weathering. The clear depletion of LREEs during the transformation from Permian to Quaternary bauxite was controlled mainly by the evolution of REE minerals. During the Permian bauxite ore-forming stage, the favorable alkaline and oxidizing environment resulted in large-scale precipitation of LREE-enriched bastnäsite and parisite. In contrast, during the Quaternary ore-forming stage, changes in pH and Eh conditions resulted in the dissolution of bastnäsite and parisite (Liu et al., 2012). Small quantities of REEs re-precipitated in cerianite and rhabdophane, while a greater quantity was lost from the system through weathering processes. This REE-loss was the major contributing factor to the overall mass change depletion of the REEs in the transformation from Permian to Quaternary bauxite.

The present results indicate that REE behavior during weathering was not conservative and was complex, with clear differentiation of some elements throughout the weathering profile. This complexity is

**Fig. 7.** Backscattered electron micrographs of REE minerals in the bauxite ores: (a) bastnäsite-(Ce) in a specific zone in an ooid, Permian Xinxu bauxite ore; (b) parisite-(Nd) fragments with dissolved edges, dispersed in the matrix of the Quaternary Xinxu bauxite ore; (c) bastnäsite-(Ce) grains and aggregates in the core of an ooid in the Permian Longhe bauxite ore; (d) bastnäsite-(Ce) grains dispersed in the matrix of the Permian Longhe bauxite ore; (e) rhabdophane and goethite vein cross-cutting Permian bauxite ore that is composed mainly of chamosite and diaspore in the Longhe bauxite deposit; (f) rhabdophane grains and aggregates concentrated at the margin of a goethite vein; (g) cerianite, Mn–Al hydroxides, and goethite vein cross-cutting Permian bauxite ore that is composed mainly of chamosite and diaspore in the Tianyang bauxite deposit; (h) cerianite concentrated at the margins of Mn–Al hydroxides veins and between Mn–Al hydroxides and Al-goethite veins.

**Table 3**
Electron probe X-ray microanalyses (wt.%) of bastnäsite and rhabdophane in sample LP-1 from the Longhe bauxite deposit.

| Plot | Bastnäsite-(Ce) | | | | | Rhabdophane | | | |
|---|---|---|---|---|---|---|---|---|---|
| | Plot-1 | Plot-2 | Plot-3 | Plot-4 | Plot-5 | Plot-6 | Plot-7 | Plot-8 | Plot-9 |
| F | 7.55 | 6.71 | 7.89 | 6.58 | 6.75 | b.d.l. | b.d.l. | b.d.l. | b.d.l. |
| $Na_2O_3$ | b.d.l. | b.d.l. | 0.23 | b.d.l. | b.d.l. | b.d.l. | b.d.l. | b.d.l. | b.d.l. |
| MgO | b.d.l. | b.d.l. | b.d.l. | b.d.l. | b.d.l. | b.d.l. | 0.21 | b.d.l. | b.d.l. |
| $Al_2O_3$ | b.d.l. | 0.94 | 3.11 | 1.06 | 3.03 | 3.02 | 2.96 | 4.88 | 8.39 |
| $SiO_2$ | 0.30 | 0.46 | 2.10 | 0.68 | 1.20 | 0.31 | 1.38 | 0.61 | 3.32 |
| CaO | 2.29 | 2.14 | 2.63 | 2.64 | 2.22 | 3.87 | 3.48 | 3.54 | 2.49 |
| $TiO_2$ | b.d.l. | b.d.l. | b.d.l. | b.d.l. | b.d.l. | b.d.l. | 0.22 | b.d.l. | 0.41 |
| MnO | b.d.l. | b.d.l. | b.d.l. | 0.16 | b.d.l. | b.d.l. | b.d.l. | b.d.l. | b.d.l. |
| $Fe_2O_3$ | b.d.l. | b.d.l. | b.d.l. | b.d.l. | b.d.l. | 2.90 | 10.68 | 4.21 | 16.94 |
| FeO | 5.76 | 6.44 | 7.96 | 6.78 | 12.19 | b.d.l. | b.d.l. | b.d.l. | b.d.l. |
| $P_2O_5$ | b.d.l. | b.d.l. | b.d.l. | b.d.l. | b.d.l. | 24.46 | 19.66 | 18.72 | 16.75 |
| $Y_2O_3$ | 1.16 | 1.14 | 0.31 | 0.85 | 0.72 | 2.80 | 1.55 | 1.98 | 0.45 |
| $La_2O_3$ | 7.02 | 5.46 | 5.49 | 7.94 | 8.98 | 8.47 | 7.30 | 7.85 | 7.70 |
| $Ce_2O_3$ | 25.25 | 23.68 | 23.13 | 24.70 | 27.63 | 24.87 | 23.48 | 25.63 | 23.81 |
| $Pr_2O_3$ | 7.25 | 7.39 | 7.89 | 6.28 | 2.79 | 2.58 | 3.71 | 4.59 | 4.34 |
| $Nd_2O_3$ | 10.41 | 9.86 | 8.91 | 9.56 | 8.19 | 10.14 | 8.16 | 8.88 | 7.14 |
| $Sm_2O_3$ | 2.77 | 3.06 | 2.71 | 3.17 | 1.06 | b.d.l. | 2.05 | 2.14 | 2.09 |
| $Eu_2O_3$ | 1.11 | 0.91 | 0.94 | 1.03 | b.d.l. | b.d.l. | b.d.l. | 0.72 | b.d.l. |
| $Gd_2O_3$ | 4.15 | 2.35 | 3.39 | 3.74 | 1.59 | b.d.l. | 2.00 | 3.44 | 1.65 |
| $Tb_2O_3$ | 0.50 | b.d.l. | 1.31 | 0.80 | b.d.l. | b.d.l. | b.d.l. | 1.60 | b.d.l. |
| $Dy_2O_3$ | 1.49 | b.d.l. | 2.08 | 1.98 | b.d.l. | b.d.l. | b.d.l. | 2.34 | 1.73 |
| $Ho_2O_3$ | b.d.l. | b.d.l. | 1.38 | b.d.l. | b.d.l. | b.d.l. | b.d.l. | 2.43 | b.d.l. |
| $Er_2O_3$ | b.d.l. | b.d.l. | 0.67 | b.d.l. | b.d.l. | b.d.l. | b.d.l. | b.d.l. | b.d.l. |
| $Tm_2O_3$ | 1.76 | b.d.l. | b.d.l. | b.d.l. | 0.96 | b.d.l. | b.d.l. | 2.77 | b.d.l. |
| $Yb_2O_3$ | 0.78 | b.d.l. | 0.43 | 0.76 | b.d.l. | b.d.l. | 0.63 | 0.71 | 0.92 |
| Total | 72.31 | 63.83 | 74.66 | 72.14 | 70.55 | 83.42 | 87.46 | 97.50 | 98.16 |
| $REE_2O_3$ | 63.96 | 53.85 | 58.64 | 60.81 | 51.92 | 48.86 | 48.88 | 65.08 | 49.83 |
| $REE_2O_3$/CaO | 27.93 | 25.16 | 22.30 | 23.03 | 23.39 | 12.63 | 14.05 | 18.38 | 20.01 |
| Atomic ratios calculated to | | | | | | | | | |
| | (O, F) = 4 | | | | | | | | |
| REE[a] | 0.91 | | 0.69 | | 0.97 | 0.90 | | 0.84 | |
| Ca | 0.10 | | 0.08 | | 0.13 | 0.12 | | 0.11 | |
| F | 0.95 | | 0.75 | | 1.15 | 0.85 | | 0.95 | |
| C | 1.03 | | 1.26 | | 0.92 | 1.06 | | 1.08 | |

[a] REE represents the sum of the atomic ratios of all rare earth elements. To obtain more precise atomic ratios of REE, F, Ca, and C, the oxides $Al_2O_3$, $SiO_2$, FeO, and $TiO_2$ were distributed to $REE_2O_3$, CaO, and F according to their proportions. $CO_2$ used for the calculation was calculated to sum of 100%.

further reflected in the observation that the species of REE-bearing minerals in parent rocks and the environmental conditions (pH and Eh) during weathering are the important factors influencing REE behavior during weathering.

### 6.2.2. Implications for the formation of bauxite in western Guangxi

Western Guangxi is the site of a carbonate platform in the Youjiang basin that was uplifted at the end of the middle Permian (Deng et al., 2010; Liu et al., 2010; Wang et al., 2011). Subaerial exposure of the platform lasted for ca. 3 Ma, during which time large-scale bauxite deposits were formed (Yu et al., 2014). This suggests that the surface environment was dominated by intensively acidic and oxidizing conditions during this period, favorable for the weathering/dissolution of minerals. The formation of churchite during this period further confirms this inference.

Subsequently, with rising groundwater, the conditions became reduced and alkaline, especially in karstic depressions (Liu et al., 2012). The prepared bauxitic materials were transported into karstic depressions by surface water, forming the Permian bauxite ore. The occurrence of bastnäsite and parisite with different textures and in different locations within the bauxite ore, and the presence of diaspore, amesite, and chamosite as the major mineral phases in the ore, suggest that the conditions of ore formation were reduced and alkaline (Figs. 8a and 9).

The Permian bauxite ore was folded and uplifted during the Mesozoic, and was again subjected to weathering in the Quaternary (Liu et al., 2012; Yu et al., 2014). The genesis of minerals in the Quaternary bauxite ore suggests that oxidizing conditions (Eh > 0) and variable pH (9.0 > pH > 4.5) were dominant in the western Guangxi at this time (Liu et al., 2012) (Figs. 8b and 9). The common dissolution of REE–fluorocarbonates and chamosite in the ore indicates that the conditions at the surface of the exposed Permian bauxite ore were dominated by pH = 4.5–6.0 and Eh > 2 (Fig. 8c and d). Mass change calculations reveal that most of the REEs were released

**Table 4**
Electron probe X-ray microanalyses (wt.%) of cerianite, Mn–Al hydroxides, and goethite in sample TP-3 from the Tianyang bauxite deposit.

| Plot | Cerianite | | | | Mn–Al hydroxides | | | Goethite |
|---|---|---|---|---|---|---|---|---|
| | Plot-1 | Plot-2 | Plot-3 | Plot-4 | Plot-5 | Plot-6 | Plot-7 | Plot-8 |
| MgO | b.d.l. | 0.21 | b.d.l. | b.d.l. | 0.18 | b.d.l. | b.d.l. | 0.35 |
| $Al_2O_3$ | 1.74 | 3.05 | 2.69 | 2.41 | 22.08 | 23.58 | 23.14 | 15.52 |
| $SiO_2$ | 1.76 | 2.68 | 2.60 | 1.97 | 0.40 | 0.48 | 0.92 | 3.41 |
| CaO | 0.27 | 0.57 | 0.55 | 0.17 | 0.15 | 0.10 | b.d.l. | 0.17 |
| $TiO_2$ | b.d.l. | b.d.l. | b.d.l. | 0.17 | b.d.l. | b.d.l. | b.d.l. | 0.36 |
| MnO | b.d.l. | 1.51 | 1.83 | b.d.l. | 45.04 | 47.34 | 46.60 | 0.65 |
| $Fe_2O_3$ | 1.91 | 2.10 | 2.93 | 2.15 | 3.58 | 3.22 | 3.27 | 59.18 |
| $P_2O_5$ | b.d.l. | b.d.l. | 0.87 | b.d.l. | b.d.l. | b.d.l. | b.d.l. | b.d.l. |
| $Y_2O_3$ | b.d.l. | b.d.l. | 0.45 | b.d.l. | b.d.l. | b.d.l. | b.d.l. | b.d.l. |
| $Ce_2O_3$ | 81.48 | 74.47 | 81.35 | 84.87 | b.d.l. | b.d.l. | b.d.l. | b.d.l. |
| Total | 87.16 | 84.59 | 93.27 | 91.74 | 71.43 | 74.72 | 73.93 | 79.64 |

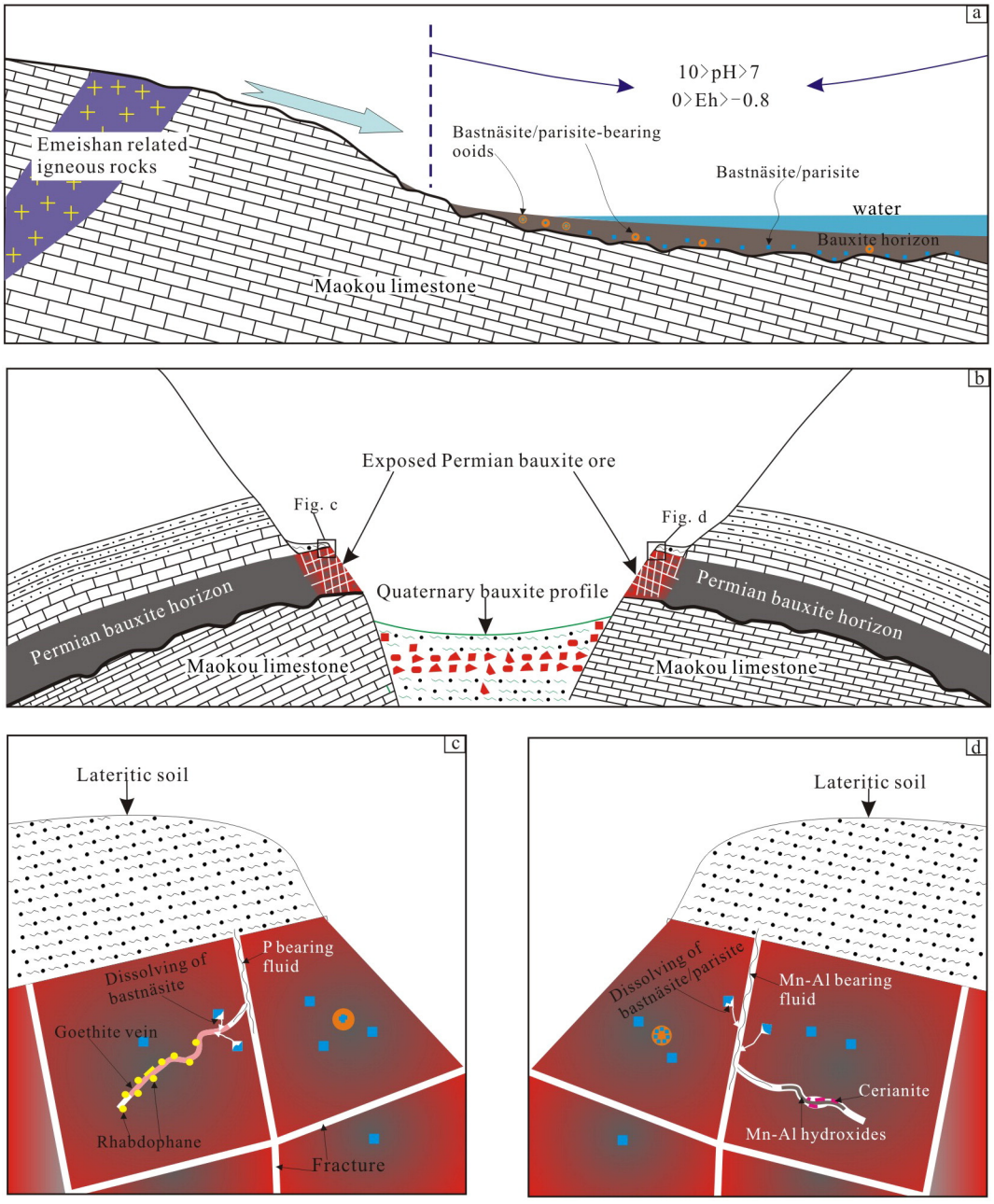


**Fig. 8.** Schematic diagrams showing the most likely scenario for the formation and evolution of the western Guangxi bauxite, and the genesis of REE minerals.

from the system through weathering processes. A small amount of the released REEs were not leached away from the system, but instead encountered weakly oxidizing and acidic conditions within fractures in the Permian bauxite ore, forming rhabdophane, while some of the $Ce^{3+}$ released from the REE–fluorocarbonates was oxidized by Mn–Al hydroxides to $Ce^{4+}$ and formed cerianite in fractures (Fig. 8c and d).

## 7. Conclusions

Five REE minerals have been identified in the western Guangxi karstic bauxite. The churchite formed during Permian weathering, and the bastnäsite and parisite formed during the Permian bauxite-forming stage and are characterized by variable REE compositions. Bastnäsite-(Ce), parisite-(Ce), and parisite-(Nd) were identified, reflecting compositional distinctions in the source material from different primary weathering profiles. Both cerianite and rhabdophane precipitated during Quaternary weathering. The REEs in these minerals originated mainly from the dissolution of bastnäsite and parisite that formed during the Permian bauxite-forming stage. This dissolution was considered to cause the removal of nearly all of the REEs during the transformation from Permian to Quaternary bauxite.

The genesis of the REE minerals, together with the occurrence of other minerals, suggests that intensively acidic and oxidizing conditions had developed before the formation of the Permian bauxite ore. However, it turned into reducing and alkaline conditions at the end of the Permian, favorable for the formation of large-scale bauxite. In contrast, the Quaternary transformation stage was dominated by variable pH and Eh conditions, and by acidic (pH = 4–6) and oxidizing (Eh > 2) conditions at the surface of the exposed Permian bauxite ore.

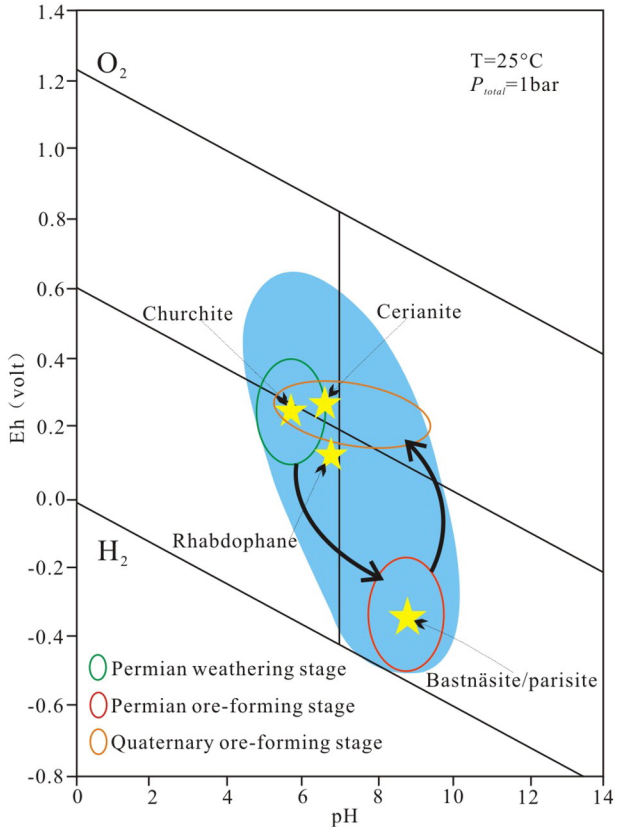


**Fig. 9.** Stability (Eh–pH) diagram showing the overall formation environment of karstic bauxite (blue area; Liu et al., 2013); the conditions during the Permian weathering stage, the Permian ore-forming stage (Liu et al., 2012), and the Quaternary ore-forming stage (Liu et al., 2012); and the conditions during the growth of parisite (Mongelli, 1997; Wang et al., 2010), bastnäsite (Maksimovic and Pantó, 1996; Li et al., 2013), rhabdophane (Berger et al., 2014), cerianite (Mongelli, 1997), and churchite (Wang et al., 2010).

## Acknowledgments

This research was jointly supported by the National Natural Science Foundation of China (No. 41202061) and the National Basic Research Programs (Nos. 2015CB452602, 2009CB421008).

## References

Appelo, C.A.J., Postma, D., 1993. Geochemistry, Groundwater and Pollution. Balkema, Rotterdam (536 pp.).
Banfield, J.F., Eggleton, R.A., 1989. Apatite replacement and rare-earth mobilization, fractionation, and fixation during weathering. Clays Clay Miner. 37, 113–127.
Bárdossy, G., 1982. Karst bauxites, bauxite deposits on carbonate rocks. Dev. Econ. Geol. 14, 1–441.
Bárdossy, G., Pantó, G., Várhegyi, G., 1976. Rare metals of Hungarian bauxites and conditions of their utilizations. Travaux ICSOBA 13, 221–231.
Bau, M., 1999. Scavenging of dissolved yttrium and rare earths by precipitating iron oxyhydroxide: experimental evidence for Ce oxidation, Y–Ho fractionation, and lanthanide tetrad effect. Geochim. Cosmochim. Acta 63, 67–77.
Berger, A., Janots, E., Gnos, E., Frei, R., Bernier, F., 2014. Rare earth element mineralogy and geochemistry in a laterite profile from Madagascar. Appl. Geochem. 41, 218–228.
Boulangé, B., Bouzat, G., Pouliquen, M., 1996. Mineralogical and geochemical characteristics of two bauxitic profiles, Fria, Guinea Republic. Mineral. Deposita 3, 432–438.
Braun, J.J., Pagel, M., Muller, J.P., Bilong, P., Michard, A., Guillet, B., 1990. Cerium anomalies in lateritic profiles. Geochim. Cosmochim. Acta 54, 781–795.
Braun, J.J., Pagel, M., Herbillon, A., Rosin, C., 1993. Mobilization and redistribution of REE and thorium in a syenitic lateritic profile — a mass-balance study. Geochim. Cosmochim. Acta 57, 4419–4434.
Braun, J.J., Viers, J., Dupré, B., Polve, M., Ndam, J., Müller, J.P., 1998. Solid/liquid REE fractionation in the lateritic system of Goyoum, east Cameroon. The implication for the present dynamics of the soil covers of the humid tropical regions. Geochim. Cosmochim. Acta 62, 273–299.
Cai, J.X., Zhang, K.J., 2009. A new model for the Indochina and South China collision during the Late Permian to the Middle Triassic. Tectonophysics 467, 35–43.
Calagari, A.A., Abedini, A., 2007. Geochemical investigations on Permo-Triassic auxite horizon at Kanisheeteh, east of Bukan, West-Azarbaidjan, Iran. J. Geochem. Explor. 94, 1–18.
Deng, J., Wang, Q.F., Yang, S.J., Liu, X.F., Zhang, Q.Z., Yang, L.Q., Yang, Y.H., 2010. Genetic relationship between the Emeishan plume and the bauxite deposits in Western Guangxi, China: constraints from U–Pb and Lu–Hf isotopes of the detrital zircons in bauxite ores. J. Asian Earth Sci. 37, 412–424.
Deng, J., Wang, Q.F., Xiao, C.H., Yang, L.Q., Liu, H., Gong, Q.J., Zhang, J., 2011. Tectonic–magmatic–metallogenic system, Tongling ore cluster region, Anhui Province, China. Int. Geol. Rev. 53, 449–476.
Deng, J., Wang, Q.F., Li, G.J., Li, C.S., Wang, C.M., 2014a. Tethys tectonic evolution and its bearing on the distribution of important mineral deposits in the Sanjiang region, SW China. Gondwana Res. 26, 419–437.
Deng, J., Wang, Q.F., Li, G.J., Santosh, M., 2014b. Cenozoic tectono-magmatic and metallogenic processes in the Sanjiang region, southwestern China. Earth-Sci. Rev. 138, 268–299.
Deng, J., Wang, Q.F., Li, G.J., Zhao, Y., 2015a. Structural control and genesis of the Oligocene Zhenyuan orogenic gold deposit, SW China. Ore Geol. Rev. 65, 42–54.
Deng, J., Wang, Q.F., Li, G.J., Hou, Z.Q., Jiang, C.Z., Danyushevsky, L., 2015b. Geology and genesis of the giant Beiya porphyry–skarn gold deposit, northwestern Yangtze Block, China. Ore Geol. Rev. 70, 457–485.
Du, Y.S., Huang, H.W., Huang, Z.Q., Xu, Y.J., Yang, J.H., Huang, H., 2009. Basin translation from Late Paleozoic to Triassic of Youjiang Basin and its tectonic significance. Geol. Sci. Technol. Inform. 28 (6), 10–15 (in Chinese with English abstract).
Duddy, I.R., 1980. Redistribution and fractionation of rare earth and other elements in a weathering profile. Chem. Geol. 30, 363–381.
He, B., Xu, Y.G., Chung, S.L., Xiao, L., Wang, Y., 2003. Sedimentary evidence for a rapid, kilometer-scale crustal doming prior to the eruption of the Emeishan flood basalts. Earth Planet. Sci. Lett. 213, 391–405.
He, B., Xu, Y.G., Guan, J.P., Zhong, Y.T., 2010. Paleokarst on the top of the Maokou Formation: further evidence for domal crustal uplift prior to the Emeishan flood volcanism. Lithos 119, 1–9.
Hukuo, K., Hikichi, Y., 1979. Syntheses of rare earth orthophosphates ($RPO_4.nH_2O$, R = La–Yb, n = 0–2). Bull. Nagoya Inst. Technol. 31, 175–182.
Johannesson, K.H., Stetzenbach, J.K., Hodge, V.F., 1995. Speciation of the rare earth element neodymium in ground waters of the Nevada Test Site and Yucca Mountain and implications for actinide solubility. Appl. Geochem. 10 (5), 565–572.
Johannesson, K.H., Stetzenbach, J.K., Hodge, V.F., Lyons, W.B., 1996. Rare earth element complexation behavior in circumneutral pH ground waters: assessing the role of carbonate and phosphate ions. Earth Planet. Sci. Lett. 139 (1–2), 305–319.
Karadağ, M.M., Küpeli, Ş., Arýk, F., Ahmet, A., Veysel, Z., Döyen, A., 2009. Rare earth element (REE) geochemistry and genetic implications of the Mortaşbauxite deposit (Seydişehir/Konya—Southern Turkey). Chem. Erde-Geochem. 69, 143–159.
Laskou, M., Andreou, G., 2003. Rare earth elements distribution and REE-minerals from the Parnassos–Ghiona bauxite deposits, Greece. In: Eliopoulos, D., et al. (Eds.), Mineral Exploration and Sustainable Development, 7th Biennial SGA Meeting, Athens. Mill Press, Rotterdam, pp. 89–92.
Li, Z.H., Din, J., Xu, J.S., Liao, C.G., Yin, F.G., Lu, T., Cheng, L., Li, J.M., 2013. Discovery of the REE minerals in the Wulong–Nanchuan bauxite deposits, Chongqing, China: insights on conditions of formation and processes. J. Geochem. Explor. 133, 88–102.
Liu, P., 1994. On the bauxite in Guizhou province—IV. Patterns of rare elements and rare earth elements in bauxite in mineralization belts from the central Guizhou to Southern Sichuan. Guizhou Geol. 11 (3), 179–186 (in Chinese with English abstract).
Liu, X.F., Wang, Q.F., Deng, J., Zhang, Q.Z., Sun, S.L., Meng, J.Y., 2010. Mineralogical and geochemical investigations of the Dajia Salento-type bauxite deposits, western Guangxi, China. J. Geochem. Explor. 105, 137–152.
Liu, X.F., Wang, Q.F., Zhang, Q.Z., Feng, Y.W., Cai, S.H., 2012. Mineralogical characteristics of the superlarge Quaternary bauxite deposits in Jingxi and Debao counties, western Guangxi, China. J. Asian Earth Sci. 52, 53–62.
Liu, X.F., Wang, Q.F., Feng, Y.W., Li, Z.M., Cai, S.H., 2013. Genesis of the Guangou karstic bauxite deposit in western Henan, China. Ore Geol. Rev. 55, 162–175.
Liu, Y., Chen, Z.Y., Yang, Z.S., Sun, X., Zhu, Z.M., Zhang, Q.C., 2015a. Mineralogical and geochemical studies of brecciated ores in the Dalucao REE deposit, Sichuan Province, southwestern China. Ore Geol. Rev. 70, 613–636.
Liu, Y., Zhu, Z.M., Chen, C., Zhang, S.P., Sun, X., Yang, Z.S., Liang, W., 2015b. Geochemical and mineralogical characteristics of weathered ore in the Dalucao REE deposit, Mianning-Dechang REE Belt, western Sichuan Province, southwestern China. Ore Geol. Rev. 71, 437–456.
Ma, L., Jin, L., Brantely, S.L., 2011. How mineralogy and slope aspect affect REE release and fractionation during shale weathering in the Susquehanna/Shale Hills Critical Zone Observatory. Chem. Geol. 290, 31–49.
MacLean, W.H., Barrett, T.J., 1993. Lithogeochemical techniques using immobile elements. Geochem. Explor. 48, 109–133.
MacLean, W.H., Kranidiotis, P., 1987. Immobile elements as monitors of mass transfer in hydrothermal alteration; Phelps Dodge massive sulfide deposit, Matagami, Quebec. Econ. Geol. 82, 951–962.
MacLean, W.H., Bonavia, F.F., Sanna, G., 1997. Argillite debris converted to bauxite during karst weathering: evidence from immobile element geochemistry at the Olmedo Deposit, Sardinia. Mineral. Deposita 32, 607–616.
Maksimovic, Z.J., Pantó, G., 1983. Mineralogy of yttrium and lanthanide elements in karstic bauxite deposits. Travaux ICSOBA 18, 191–200.
Maksimovic, Z.J., Pantó, G., 1996. Authigenic rare earth minerals in karst-bauxites and karstic nickel deposits rare earth minerals. In: Adrian, P.J., Famces, W., Williams, C.T. (Eds.), Rare Earth Minerals Chemistry, Origin and Ore Deposits 3, pp. 257–309.

Mameli, P., Mongelli, G., Oggiano, G., Dinelli, E., 2007. Geological, geochemical and mineralogical features of some bauxite deposits from Nurra (Western Sardinia, Italy): insights on conditions of formation and parental affinity. Int. J. Earth Sci. 96, 887–902.
Marsh, J.S., 1991. REE fractionation and Ce anomalies in weathered Karoo dolerite. Chem. Geol. 90, 189–194.
Mei, M.X., Ma, Y.S., Deng, J., Chu, H.M., Zheng, K.B., 2007. Sequence-stratigraphic succession and paleogeography of the Yunnan–Guizhou–Guangxi and adjacent region. Sci. China 37 (5), 605–617 (in Chinese with English abstract).
Mongelli, G., 1997. Ce-anomalies in the textural components of Upper Cretaceous karst bauxites from the Apulian carbonate platform (southern Italy). Chem. Geol. 140, 69–79.
Mongelli, G., Boni, M., Buccione, R., Sinisi, R., 2014. Geochemistry of the Apulian karst bauxites (southern Italy): chemical fractionation and parental affinities. Ore Geol. Rev. 63, 9–21.
Mordberg, L.E., 1996. Geochemistry of trace elements in Paleozoic bauxite profiles in northern Russia. J. Geochem. Explor. 57, 187–199.
Murakami, T., Utsunomiya, S., Imazu, Y., Prasad, N., 2001. Direct evidence of late Archean to early Proterozoic anoxic atmosphere from a product of 2.5 Ga old weathering. Earth Planet. Sci. Lett. 184, 523–528.
Nesbitt, H.W., 1979. Mobility and fractionation of rare earth elements during weathering of a granodiorite. Nature 279, 206–210.
Ohta, A., Kawabe, I., 2001. REE(III) adsorption onto Mn oxide (δ-$MnO_2$) and Fe oxyhydroxide: Ce(III) oxidation by δ-$MnO_2$. Geochim. Cosmochim. Acta 65, 695–703.
Rankin, P.C., Childs, C.W., 1976. Rare earth elements in iron manganese concretions from some New Zealand soils. Chem. Geol. 18, 54–64.
Sanematsu, K., Kon, Y., Imai, A., Watanabe, K., Watanabe, Y., 2013. Geochemical and mineralogical characteristics of ion-adsorption type REE mineralization in Phuket, Thailand. Mineral. Deposita 48, 437–451.
Sawka, W.N., Banfield, J.F., Chappell, B.W., 1986. A weathering elated origin of widespread monazite in S-type granites. Geochim. Cosmochim. Acta 50, 171–175.
Steinberg, M., Courtois, C., 1976. Le comportement des terresrares au cours de l'alteration et ses consequences. Bull. Soc. Geol. Fr. 1, 13–20.
Stille, P., Pierret, M.C., Steinmann, M., Chabaux, F., Boutin, R., Aubert, D., Pourcelot, L., Morvan, G., 2009. Impact of atmospheric deposition, biogeochemical cycling and water–mineral interaction on REE fractionation in acidic surface soils and soil water (the Strengbach case). Chem. Geol. 264, 173–186.
Sun, Y., Lai, X., Wignall, P.B., Widdowson, M., Ali, J.R., Jiang, H., Wang, W., Yan, C., Bond, D.P.G., Védrine, S., 2010. Dating the onset and nature of the Middle Permian Emeishan large igneous province eruptions in SW China using conodont biostratigraphy and its bearing on mantle plume uplift models. Lithos 119, 20–33.
Taunton, A.E., Welch, S.A., Banfield, J.F., 2000. Microbial controls on phosphate and lanthanide distributions during granite weathering and soil formation. Chem. Geol. 169, 371–382.
Topp, S.E., Salbu, B., Roaldset, E., Jorgensen, P., 1984. Vertical distribution of trace elements in laterite soil Suriname. Chem. Geol. 47, 865–903.
Wang, Q.F., Deng, J., Liu, X.F., Zhang, Q.Z., Sun, S.L., Jiang, C.Z., Zhou, F., 2010. Discovery of the REE minerals and its geological significance in the Quyang bauxite deposit, West Guangxi, China. J. Asian Earth Sci. 39, 701–712.
Wang, Q.F., Deng, J., Zhang, Q.Z., Liu, H., Liu, X.F., Wan, L., Li, N., Wang, Y.R., Jiang, C.Z., Feng, Y.W., 2011. Orebody vertical structure and implications for ore-forming processes in the Xinxu bauxite deposit, Western Guangxi, China. Ore Geol. Rev. 39, 230–244.
Welch, S.A., Christy, A.C., Isaacson, L., Kirste, D., 2009. Mineralogical control of rare earth elements in acid sulfate soils. Geochim. Cosmochim. Acta 73, 44–64.
Wu, G.Y., Zhong, D.L., Zhang, Q., Ji, J.Q., 1999. Babu-Phu Ngu ophiolites: a geological record of paleotethyan ocean bordering China and Vietnam. Gondwana Res. 2, 554–557.
Wu, G.Y., Wu, H.R., Zhong, D.L., Kuang, G.D., Ji, J.Q., 2000. Volcanic rocks of paleotethyan oceanic island and island-arc bordering Yunnan and Guangxi, China. Mod. Geol. 14, 393–400 (in Chinese with English abstract).
Wu, G.Y., Ji, J.Q., He, S.D., Zhong, D.L., 2002. Early Permian magmatic arc in Pingxiang, Guangxi and its tectonic implications. J. Mineral. Petrol. 22 (3), 61–65 (in Chinese with English abstract).
Yang, J.H., Cawood, P.A., Du, Y.S., Huang, H., Hu, L.S., 2012a. Detrital record of Indosinian mountain building in SW China: provenance of the Middle Triassic turbidites in the Youjiang Basin. Tectonophysics 574–575, 105–117.
Yang, J.H., Cawood, P.A., Du, Y.S., Huang, H., Huang, H.W., Tao, P., 2012b. Large Igneous Province and magmatic arc sourced Permian–Triassic volcanogenic sediments in China. Sediment. Geol. 261–262, 120–131.
Yin, J.W., Shao, X.K., Yang, H.T., Piao, T.X., Xu, H.M., Wang, J., 2013. Radioactive mineral characteristics of Boziguoer alkaline rocks in Baicheng, Xinjiang. Mineral Deposits 32 (2), 337–352 (in Chinese with English abstract).
Yu, W.C., Wang, R.H., Zhang, Q.L., Du, Y.S., Chen, Y., Liang, Y.P., 2014. Mineralogical and geochemical evolution of the Fusui bauxite deposit in Guangxi, South China: from the original Permian orebody to a Quarternary Salento-type deposit. J. Geochem. Explor. 146, 75–88.